

Interferometry of black holes with Hawking radiation

Yasusada Nambu*

*Department of Physics, Graduate School of Science,
Nagoya University, Chikusa, Nagoya 464-8602, Japan*

Sousuke Noda†

National Institute of Technology, Miyakonojo College, Miyakonojo 885-8567, Japan and

*Center for Gravitation and Cosmology,
College of Physical Science and Technology,
Yangzhou University, Yangzhou 225009, China*

(Dated: February 3, 2022 ver 2.0)

Abstract

We investigate the wave optical imaging of black holes with Hawking radiation. The spatial correlation function of Hawking radiation is expressed in terms of transmission and reflection coefficients for scalar wave modes and evaluated by numerically summing over angular quantum numbers for the Unruh-Hawking state of the Kerr-de Sitter black hole. Then, wave optical images of an evaporating black hole are obtained by the Fourier transformation of the spatial correlation function. For short wavelength, the image of the black hole with the outgoing mode of the Unruh-Hawking state has the appearance of a star with its surface given by the photon sphere. It is found that interference between incoming modes from the cosmological horizon and reflected modes due to the scattering of the black hole can enhance brightness of images in the vicinity of the photon sphere. For a long wavelength, the entire field of view is bright, and the emission region of Hawking radiation cannot be identified.

Keywords: Hawking radiation; wave optics; van Cittert-Zernike theorem; photon sphere; Kerr-de Sitter black hole

*Electronic address: nambu@gravity.phys.nagoya-u.ac.jp

†Electronic address: snoda@cc.miyakonojo-nct.ac.jp

Contents

I. Introduction	2
II. Van Cittert-Zernike theorem and wave optical imaging	5
A. Van Cittert-Zernike theorem	5
B. Qubit detector and response functions	6
III. Hawking radiation in Kerr-de Sitter spacetime	8
A. Basic formulas	8
B. Correlation function	12
IV. Evaluation of transmission and reflection coefficients	15
V. Imaging of black holes with Hawking radiation	17
A. Detail of imaging method and an example with a simple model	17
B. Black hole images	20
1. Images for $a = 0$ (Schwarzschild case)	20
2. Images for $a = 1/10$ (slowly rotating case)	24
3. Images for $a = 1$ (fast-rotating case)	27
4. Images of G_1 and emission region of Hawking radiation	30
VI. Summary	31
Acknowledgments	32
A. Van Cittert-Zernike theorem in de Sitter spacetime	32
References	33

I. INTRODUCTION

In general relativity, a black hole is defined as a spacetime region surrounded by the event horizon, from which no light signals can escape to the null infinity. There are several possibilities for the formation of black holes in our universe: the gravitational collapse of stars, coalescence of compact stars, phase transition in the early universe, and so on. An important concept characterizing black holes is the photon sphere, which is defined as a surface composed of bounded null geodesics [1–3]. For a rotating black hole, there are two circular photon orbits in the equatorial plane, and their radii differ depending on the signs of the photon angular momentum. There are also other bounded photon orbits, which depart from the equatorial plane¹. We call a set of bounded photon orbits as a “photon sphere” in this paper. When considering the propagation of ingoing null rays towards a black hole, null rays that cross the photon sphere cannot escape the photon sphere. From a distant

¹ The radius of a bounded photon orbit is determined by combination of parameters $(L_z/E, C/E^2)$, where C is the Carter constant, L_z is the z component of the angular momentum and E is the energy of photon [2]. The orbit forms a shell-like structure (photon shell) [3].

observer, a set of projected bounded photon orbits on a far observer’s view plane appears as a distorted disk that corresponds to the black hole shadow for a rotating black hole [2].

Astrophysical black holes are associated with the surrounding gases showing light emission. Thus, the photon sphere of a black hole can be visible as the rim of a dark shadow region in bright background emission. Indeed, recent observation of the central region of M87 with very large baseline interferometry (VLBI) reported an image of the photon sphere associated with the central supermassive black hole [4–9]. As the apparent angular sizes of black hole candidates are very small from the Earth, the key technology to resolve black hole shadows by observation is aperture synthesis; by combining several independent telescopes on the Earth, the effective size of the aperture can be increased, making it possible to resolve black holes with very small apparent sizes. The image reconstruction of black holes is performed based on a property of the wave optics known as the van Cittert-Zernike theorem [10–12], which states that the Fourier transformation of the first-order degrees of coherence (interferometric fringe pattern) in an observer’s screen provides an intensity distribution of a source object if the spatial incoherence of the source field is assumed.

In this paper, we aim to obtain wave optical images of evaporating black holes. Owing to the quantum effect, black holes can emit thermal radiation known as Hawking radiation [13, 14], the temperature of which is proportional to the surface gravity of black hole horizons. Hence, if we detect Hawking radiation of a black hole from a spatially distant region, it is possible to reconstruct wave optical images of the evaporating black hole by applying the van Cittert-Zernike theorem. Of course, this investigation is only a theoretical thought experiment because the Hawking temperatures of astrophysical black holes are too low to detect directly. However, we expect that our analysis will provide a deeper understanding of Hawking radiation and black hole spacetimes from the viewpoint of wave optics. In particular, it may be possible to acquire information on the emission region of Hawking radiation by performing the wave optical imaging of a black hole, and this direction of investigation is related to the question “where does Hawking radiation originate?” [15, 16]. In our previous studies [17, 18], we discussed the wave optical imaging of black holes with a coherent point wave source. Interference fringes due to wave scattering by a black hole appear on the observer’s screen. By the Fourier transformation of the interference fringe, images of the Einstein ring and photon sphere are obtained. For the case of an evaporating black hole, the wave source is the black hole itself, and all the information necessary for imaging is contained in the correlation function of Hawking radiation. Concerning the quantum state of black holes, we assume the Unruh-Hawking vacuum state, which is realized as black hole formation via gravitational collapse [1, 13, 14, 19–23].

In our analysis, instead of treating the asymptotically flat Kerr spacetime, we consider the Kerr-de Sitter (KdS) spacetime because it allows the evaluation of the reflection and transmission coefficients for wave modes. As we will show, for a massless conformal scalar field that represents scalar Hawking radiation, the radial wave equation can be transformed into the Heun equation, which has four regular singular points. In this case, the outer black hole horizon and the cosmological horizon correspond to regular singular points of the Heun equation. Therefore, the asymptotic solutions at the horizon can be written with the local regular solutions of the Heun equation (local Heun function) via the Frobenius method, and it is possible to obtain the exact form of reflection and transmission coefficients in terms of the local Heun function. For the asymptotically flat Kerr spacetime, the radial wave function is represented by the confluent Heun function, which has two regular singular points and one irregular singular point, and spatial infinity corresponds to the irregular singular point.

Although we have local solutions for the outer black hole horizon, it is technically difficult to match this solution to that of infinity. Concerning this issue, Hatsuda [33] proposed a method of taking a small cosmological constant and extrapolating the value to obtain the quasi-normal frequency for the asymptotically flat black hole spacetime and further checked its validity. In the present paper, we adopt his approach and investigate Hawking radiation in the KdS spacetime with a sufficiently small value of the cosmological constant, and the effect of radiation from the cosmological horizon is not significant. The vacuum condition is imposed on the past event horizon and the past cosmological horizon of the Kruskal extended KdS spacetime. For detecting Hawking radiation, we prepare two qubit detectors to measure the spatial correlation of Hawking radiation. Then, by the Fourier transformation of the spatial correlation function, we can obtain wave optical images of black holes.

The remainder of this paper is organized as follows. In Section II, we shortly review the van Cittert-Zernike theorem and the qubit detector model. We adopt two qubit detectors as our imaging system, which can extract the spatial correlation of a wave field. In Section III, after reviewing Hawking radiation in the KdS spacetime, we present the spatial correlation function of Hawking radiation in terms of transmission and reflection coefficients for wave modes. In Section IV, we explain a numerical method to evaluate reflection and transmission coefficients. In Section V, we present images of black holes. Section VI is devoted to a summary and conclusion. We adopt units of $c = \hbar = G = 1$ throughout this paper.

II. VAN CITTERT-ZERNIKE THEOREM AND WAVE OPTICAL IMAGING

We shortly review a method of wave optical imaging based on the van Cittert-Zernike theorem [10–12] for the flat spacetime, which corresponds to asymptotically flat black hole spacetimes. We also show in the Appendix that the same form of the theorem also holds for the de Sitter case by replacing the radial coordinate in the phase factor with the tortoise coordinate of de Sitter space. Then, we review the qubit detector system, which is applicable to the detection of the spatial correlations of Hawking radiation, to employ image formation based on the van Cittert-Zernike theorem.

A. Van Cittert-Zernike theorem

Let us consider the emission of a scalar wave from a source $\rho(t, \mathbf{x})$, which possesses a random statistical property. We observe the emitted wave far from the source (Fig. 1).

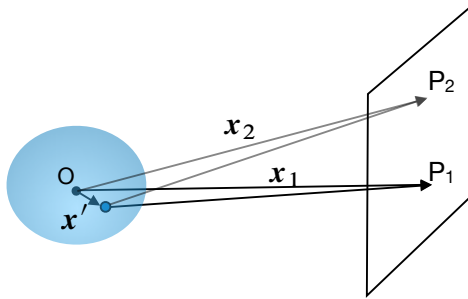


FIG. 1: A wave source is located around the origin. Detection points P_1 and P_2 are assumed to be far from the source.

We consider the scalar wave function Φ that obeys the wave equation $(\partial_t^2 - \nabla^2)\Phi = \rho(t, \mathbf{x})$. Time dependence is separated using the temporal Fourier components as

$$\Phi(t, \mathbf{x}) = \int_{-\infty}^{+\infty} d\omega e^{-i\omega t} \Phi_\omega(\mathbf{x}), \quad \rho(t, \mathbf{x}) = \int_{-\infty}^{+\infty} d\omega e^{-i\omega t} \rho_\omega(\mathbf{x}), \quad (1)$$

with $\Phi_\omega = \Phi_{-\omega}^*$, $\rho_\omega = \rho_{-\omega}^*$. The wave equation is then expressed as

$$(\nabla^2 + \omega^2)\Phi_\omega = -\rho_\omega. \quad (2)$$

The Green's function of this equation with a retarded boundary condition is

$$\mathcal{G}_\omega(\mathbf{x}, \mathbf{x}_s) = \frac{e^{i\omega|\mathbf{x}-\mathbf{x}_s|}}{4\pi|\mathbf{x}-\mathbf{x}_s|} \approx \frac{e^{i\omega(r-\mathbf{x}\cdot\mathbf{x}_s/r)}}{4\pi r}, \quad (3)$$

where $r = |\mathbf{x}|$ and we assume the detection point \mathbf{x} is far from the source region. The solution of Eq. (2) is given by $\Phi_\omega(\mathbf{x}) = \int d^3\mathbf{x}_s \mathcal{G}_\omega(\mathbf{x}, \mathbf{x}_s) \rho_\omega(\mathbf{x}_s)$. The correlation function of the scalar field is

$$\langle \Phi(t_1, \mathbf{x}_1) \Phi(t_2, \mathbf{x}_2) \rangle = \int_{-\infty}^{+\infty} d\omega e^{-i\omega(t_1-t_2)} \langle \Phi_\omega(\mathbf{x}_1) \Phi_\omega^*(\mathbf{x}_2) \rangle, \quad (4)$$

where $\langle \dots \rangle$ denotes statistical averaging and we used the stationarity condition for the scalar field $\langle \Phi_{\omega_1}(\mathbf{x}_1)\Phi_{\omega_2}(\mathbf{x}_2) \rangle \propto \delta(\omega_1 + \omega_2)$. The correlation function of the temporal Fourier component of the field is

$$\begin{aligned} G(\omega, \mathbf{x}_1, \mathbf{x}_2) &:= \langle \Phi_\omega(\mathbf{x}_1)\Phi_\omega^*(\mathbf{x}_2) \rangle = \int d^3\mathbf{x}_{s1}d^3\mathbf{x}_{s2}\mathcal{G}_\omega(\mathbf{x}_1, \mathbf{x}_{s1})\mathcal{G}_\omega^*(\mathbf{x}_2, \mathbf{x}_{s2}) \langle \rho_\omega(\mathbf{x}_{s1})\rho_\omega^*(\mathbf{x}_{s2}) \rangle \\ &= \int d^3\mathbf{x}_s\mathcal{G}_\omega(\mathbf{x}_1, \mathbf{x}_s)\mathcal{G}_\omega^*(\mathbf{x}_2, \mathbf{x}_s)I_\omega(\mathbf{x}_s), \end{aligned} \quad (5)$$

where we assumed spatial incoherency of the source field. This means that the correlation between different spatial points is zero:

$$\langle \rho_\omega(\mathbf{x}_{s1})\rho_\omega^*(\mathbf{x}_{s2}) \rangle = I_\omega(\mathbf{x}_{s1})\delta^3(\mathbf{x}_{s1} - \mathbf{x}_{s2}), \quad (6)$$

where $I_\omega(\mathbf{x}_s)$ is the intensity of the source at \mathbf{x}_s . Using (3) with $|\mathbf{x}_1| = |\mathbf{x}_2| = r$,

$$\begin{aligned} G(\omega, \mathbf{x}_1, \mathbf{x}_2) &= \frac{1}{16\pi^2r^2} \int d^3\mathbf{x}_s I_\omega(\mathbf{x}_s) \exp[-i\omega(\mathbf{x}_1 - \mathbf{x}_2) \cdot \mathbf{x}_s/r] \\ &= \frac{1}{16\pi^2r^2} \int d^2\mathbf{x}_\parallel \tilde{I}_\omega(\mathbf{x}_\parallel) e^{-i\omega\mathbf{x}_{12} \cdot \mathbf{x}_\parallel/r}, \end{aligned} \quad (7)$$

where we decompose \mathbf{x}_s as $\mathbf{x}_s = \mathbf{x}_\perp + \mathbf{x}_\parallel$, $(\mathbf{x}_1 - \mathbf{x}_2) \cdot \mathbf{x}_\perp = 0$ and $\mathbf{x}_{12} = \mathbf{x}_1 - \mathbf{x}_2$. The projected source intensity is introduced as

$$\tilde{I}_\omega(\mathbf{x}_\parallel) = \int dx_\perp I_\omega(x_\perp, \mathbf{x}_\parallel). \quad (8)$$

Ultimately, we obtain a relation between the spatial field correlation function and the spatial distribution of source intensity:

$$G(\omega, \mathbf{x}_1, \mathbf{x}_2) \propto \int d^2\mathbf{y} \tilde{I}_\omega(\mathbf{y}) \exp\left(-i\frac{\omega}{r}\mathbf{x}_{12} \cdot \mathbf{y}\right). \quad (9)$$

This formula is called the van Cittert-Zernike theorem [10–12]. Thus, we can reconstruct the distribution of the source intensity (image of the source) from the spatial field correlation function as follows:

$$\tilde{I}_\omega(\mathbf{y}) \propto \int d^2\mathbf{x}_{12} G(\omega, \mathbf{x}_1, \mathbf{x}_2) \exp\left(i\frac{\omega}{r}\mathbf{y} \cdot \mathbf{x}_{12}\right). \quad (10)$$

Even if the property of spatial incoherence of the source is unknown, $\tilde{I}_\omega(\mathbf{y})$ obtained using Eq. (10) provides one possible visualization of the source field, irrespective of the spatial incoherence of the source field.

For asymptotic de Sitter spacetimes, as we explain the Appendix, the same relation (10) holds on replacing the radial coordinate with the tortoise coordinate, provided that the impact parameters of the involved wave modes are shorter than the Hubble horizon length.

B. Qubit detector and response functions

As a measurement apparatus of the spatial correlation of Hawking radiation, we introduce two detectors interacting with Hawking radiation and obtain the field correlation through

correlation between two detectors. The detectors are assumed to have two internal levels (qubit) with the energy gap $\omega_0 > 0$. The interaction Hamiltonian between qubits and the quantum scalar field $\hat{\Phi}$ (Hawking radiation) is assumed to be

$$\hat{H}_{\text{int}} = g_1(t)(\sigma_1^+ + \sigma_1^-)\hat{\Phi}(\mathbf{x}_1(t)) + g_2(t)(\sigma_2^+ + \sigma_2^-)\hat{\Phi}(\mathbf{x}_2(t)), \quad (11)$$

where $\sigma_{1,2}^+$ and $\sigma_{1,2}^-$ are raising and lowering operators, respectively, for the detector's state and $g_{1,2}(t)$ are switching functions. The world lines of detectors are denoted by $\mathbf{x}_{1,2}(t)$. This detector system setup is often employed to investigate the entanglement harvesting of quantum fields [24–27]. In our investigation to measure the spatial correlation of Hawking radiation, two detectors are placed at the same radial coordinate far from the black hole. For the initial ground state of the detectors, after interaction with the scalar field, the detector state becomes [27, 28]

$$\rho_{12} = \begin{bmatrix} X_4 & 0 & 0 & X \\ 0 & E_1 & E_{12} & 0 \\ 0 & E_{12} & E_2 & 0 \\ X^* & 0 & 0 & 1 - E_1 - E_2 - X_4 \end{bmatrix}, \quad (12)$$

where

$$X = -2 \int_{-\infty}^{+\infty} dt_1 \int_{-\infty}^{t_1} dt_2 g_1 g_2 e^{i\omega_0(t_1+t_2)} \langle \hat{\Phi}(t_1, \mathbf{x}_1) \hat{\Phi}(t_2, \mathbf{x}_2) \rangle, \quad (13)$$

$$E_{12} = \int_{-\infty}^{+\infty} dt_1 \int_{-\infty}^{+\infty} dt_2 g_1 g_2 e^{-i\omega_0(t_1-t_2)} \langle \hat{\Phi}(t_1, \mathbf{x}_1) \hat{\Phi}(t_2, \mathbf{x}_2) \rangle, \quad (14)$$

$$E_1 = E_{12}|_{2=1}, \quad E_2 = E_{12}|_{1=2}, \quad X_4 = O(g^4). \quad (15)$$

The expectation values of field operators are taken with respect to the assumed quantum state of the scalar field. The component $E_{1,2}(\omega_0)$ represents the amount of local quantum fluctuation measured by detectors and shows the Planckian distribution for black hole cases [19, 23]. The component X represents quantum coherence between two detectors. The entanglement between two detectors can be judged by the entanglement negativity [29], which is proportional to $|X| - \sqrt{E_1 E_2}$ in the present case. Positive values of this quantity imply that two detectors are entangled and entanglement of the quantum field is measured by the detectors. Entanglement harvesting in black hole spacetimes has been investigated in several studies (BTZ case [26], Schwarzschild case [30], and Kerr case [31]). The two-point function (Wightman function) is expressed as

$$D^+(t_1, t_2, \mathbf{x}_1, \mathbf{x}_2) := \langle \hat{\Phi}(t_1, \mathbf{x}_1) \hat{\Phi}(t_2, \mathbf{x}_2) \rangle = \int_{-\infty}^{+\infty} d\omega e^{-i\omega(t_1-t_2)} G(\omega, \mathbf{x}_1, \mathbf{x}_2) \quad (16)$$

because of the stationarity of the correlation $D^+(t_1, t_2, \mathbf{x}_1, \mathbf{x}_2) = D^+(t_1 - t_2, \mathbf{x}_1, \mathbf{x}_2)$. By changing the integration variables to $x = (t_1 + t_2)/2$ and $y = (t_1 - t_2)/2$, and assuming

constant switching functions $g_1 = g_2 = g$, we obtain²

$$X = -4g^2 \int_{-\infty}^{+\infty} dx e^{2i\omega_0 x} \int_0^{+\infty} dy D^+(2y, \mathbf{x}_1, \mathbf{x}_2) \propto g^2 \delta(\omega_0), \quad (17)$$

$$E_{12} = 2g^2 \int_{-\infty}^{+\infty} dx \int_{-\infty}^{+\infty} dy e^{-2i\omega_0 y} D^+(2y, \mathbf{x}_1, \mathbf{x}_2) = 4\pi g^2 \left(\int dx \right) G(-\omega_0, \mathbf{x}_1, \mathbf{x}_2), \quad (18)$$

$$E_1 = E_{12}|_{\mathbf{x}_2=\mathbf{x}_1}, \quad E_2 = E_{12}|_{\mathbf{x}_1=\mathbf{x}_2}. \quad (19)$$

The formal expression (18) contains an infinite factor, but it should be treated with some cutoff of integration and G is replaced by the Fourier transformation with finite interval of the correlation function. Because $\omega_0 \neq 0$, we have $X = 0$ for constant switching functions. By considering the state tomography of the detector system, that is, by measuring components of the state (12), it is possible to access the component E_{12} , which is proportional to the temporal Fourier component of the Wightman function $G(\omega_0, \mathbf{x}_1, \mathbf{x}_2)$, and this quantity represents the spatial correlation of the quantum field. Therefore, the setup of two detectors can be applied as an imaging system of black holes with Hawking radiation.

III. HAWKING RADIATION IN KERR-DE SITTER SPACETIME

We shortly review Hawking radiation in the Kerr-de Sitter spacetime [1, 19–21, 23].

A. Basic formulas

We consider a massless conformal scalar field φ in the Kerr-de Sitter (KdS) spacetime. This scalar field is equivalent to the scalar mode of gravitational perturbation, which obeys the Teukolsky equation. The metric of the KdS spacetime is

$$ds^2 = -\frac{\Delta_r}{\rho^2 \chi^4} (dt - a \sin^2 \theta d\phi)^2 + \frac{\Delta_\theta}{\rho^2 \chi^4} \sin^2 \theta ((r^2 + a^2)d\phi - a dt)^2 + \rho^2 \left(\frac{dr^2}{\Delta_r} + \frac{d\theta^2}{\Delta_\theta} \right), \quad (20)$$

with

$$\Delta_r = (r^2 + a^2) \left(1 - \frac{\Lambda}{3} r^2 \right) - 2Mr, \quad \Delta_\theta = 1 + \frac{\Lambda}{3} a^2 \cos^2 \theta, \quad (21)$$

$$\rho^2 = r^2 + a^2 \cos^2 \theta, \quad \chi^2 = 1 + \frac{\Lambda}{3} a^2. \quad (22)$$

The parameters specifying this spacetime are (M, a, Λ) . The scalar field obeys the following wave equation:

$$-\nabla_\mu \nabla^\mu \varphi + \frac{1}{6} R^{(4)} \varphi = 0, \quad R^{(4)} = 4\Lambda, \quad (23)$$

2

$$G(-\omega, \mathbf{x}_1, \mathbf{x}_2) = G^*(\omega, \mathbf{x}_1, \mathbf{x}_2), \quad G(-\omega, \mathbf{x}, \mathbf{x}) = G(\omega, \mathbf{x}, \mathbf{x}).$$

where $R^{(4)}$ is the four-dimensional Ricci scalar. We introduce the tortoise coordinate r_* defined by

$$r_* = \int dr \frac{r^2 + a^2}{\Delta_r} = \frac{\log|r - r_c|}{2\kappa_c} + \frac{\log|r - r_+|}{2\kappa_+} + \frac{\log|r - r_-|}{2\kappa_-} + \frac{\log|r - r_{--}|}{2\kappa_{--}}, \quad (24)$$

where $r_{--} < 0 < r_- < r_+ < r_c$ are four roots of $\Delta_r = 0$; r_+ is the radius of the outer event horizon, and r_c is the radius of the cosmological horizon (Fig. 2). The surface gravity κ and the angular velocity Ω at these points are given by

$$\kappa_j := \kappa(r_j) = \frac{\Delta'_r(r_j)}{2\chi^2(r_j^2 + a^2)}, \quad \Omega_j = \frac{a}{r_j^2 + a^2}, \quad j = --, -, +, c, \quad (25)$$

where $' = \partial/\partial r$. The right panel of Fig. 2 shows a parameter region for a real r_+ and a real r_c in the $(\Lambda M^2, a/M)$ plane [32]. For such values of parameters, we have a Kerr black hole enclosed by a cosmological horizon.

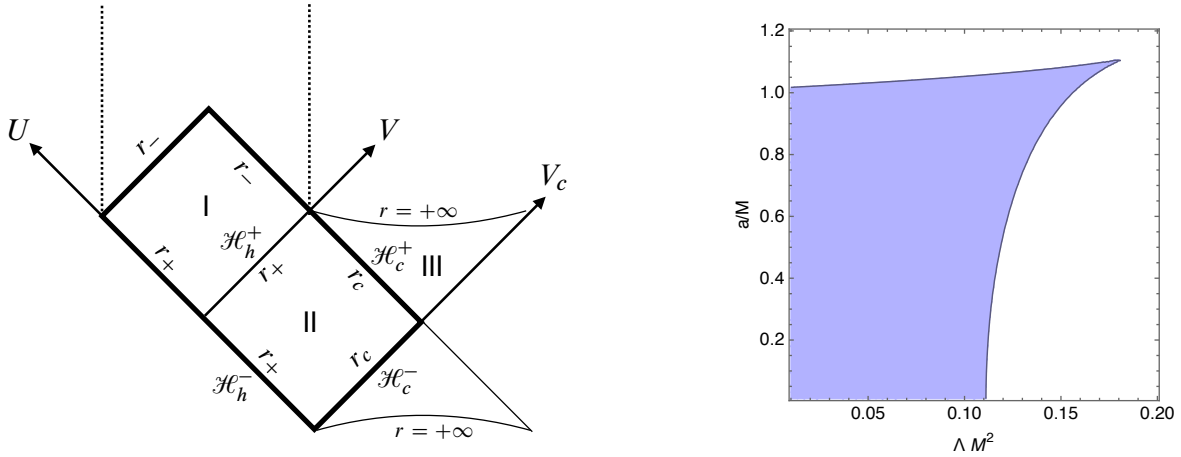


FIG. 2: Left panel: global structure of the KdS spacetime considered to investigate Hawking radiation with the Unruh-Hawking vacuum state. Dotted vertical lines represent singularity. Right panel: colored region represents the parameters for a real r_+ and a real r_c . The upper boundary is the extremal limit, where $\kappa_+ = 0$. The lower boundary corresponds to $r_+ = r_c$ (Nariai limit). Black holes with $a > 1$ (“over spinning” yet maintaining its horizon structure) are possible for $\Lambda > 0$.

The scalar field in the KdS spacetime is separated as

$$\varphi_{\omega\ell m} = \frac{R_{\omega\ell m}(r)}{\sqrt{r^2 + a^2}} S_{\omega\ell m}(\cos\theta) e^{im\phi}, \quad (26)$$

where $S_{\omega\ell m}(\cos\theta)$ is the angular wave function obeying the following equation:

$$\left[\frac{d}{d\xi} \{1 + (\chi^2 - 1)\xi^2\} (1 - \xi^2) \frac{d}{d\xi} - 2(\chi^2 - 1)\xi^2 - \frac{\chi^4 \{m - (1 - \xi^2)a\omega\}^2}{\{1 + (\chi^2 - 1)\xi^2\} (1 - \xi^2)} + \lambda_{\ell m}(a\omega, \Lambda) \right] S_{\omega\ell m}(\xi) = 0, \quad (27)$$

where $\xi = \cos \theta$ and $\lambda_{\ell m}(a\omega, \Lambda)$ is the eigenvalue of this equation. As Eq. (27) has four regular singular points, it can be written in terms of the Heun equation with an appropriate transformation [33, 34] to obtain the values of $S_{\omega \ell m}(\xi)$ for the range of $0 \leq \theta \leq \pi$ using the local Heun functions. Moreover, the eigenvalues $\lambda_{\ell m}(a\omega, \Lambda)$ are also obtained by finding the zero point of the Wronskian for the linear independent local Heun functions, which is equivalent to the regularity condition for $S_{\omega \ell m}(\xi)$ at $\theta = 0, \pi$ [33, 34]. For the eigenvalues, an analytic formula was derived in [35]. We have checked that the formula provides numerical values of $\lambda_{\ell m}$ with acceptable accuracy even for the parameter region $a\omega \sim O(1)$ with $\Lambda = 1/100$. Hence we used the analytic formula in the present study.

The radial wave function $R_{\omega \ell m}(r)$ obeys

$$\left[\frac{d^2}{dr_*^2} - V_{\omega \ell m}(r) \right] R_{\omega \ell m} = 0 \quad (28)$$

with the potential

$$V_{\omega \ell m}(r) = -\chi^4 (\omega - m\Omega)^2 + \frac{\Delta_r}{\chi^4 (r^2 + a^2)^2} \left\{ \lambda_{\ell m}(a\omega, \Lambda) + \frac{2}{3} \Lambda r^2 + (r^2 + a^2)^{1/2} \left(\frac{r \Delta_r}{(r^2 + a^2)^{3/2}} \right)' \right\}. \quad (29)$$

For investigating Hawking radiation, we consider the extended KdS spacetime shown in the left panel of Fig. 2. The Kruskal coordinates about bifurcating horizons r_+ and r_c are defined as

$$U = +\frac{e^{-\kappa_+ u}}{\kappa_+}, \quad V = \frac{e^{\kappa_+ v}}{\kappa_+} \quad \text{in region I,} \quad (30)$$

$$U = -\frac{e^{-\kappa_+ u}}{\kappa_+}, \quad V = \frac{e^{\kappa_+ v}}{\kappa_+}, \quad V_c = -\frac{e^{-\kappa_c v}}{\kappa_c} \quad \text{in region II,} \quad (31)$$

$$V_c = \frac{e^{-\kappa_c v}}{\kappa_c} \quad \text{in region III,} \quad (32)$$

where $u = t - r_*$ and $v = t + r_*$.

As the state of Hawking radiation, we adopt the Unruh-Hawking vacuum state. The condition for the quantum state is presented in the subsection B of the present section. We shortly comment on three typical vacuum states for quantum fields in the asymptotically flat static black hole spacetime. The Boulware vacuum state is defined by taking positive frequency modes for the past and future null infinities. This vacuum state shows no particle emission from a black hole. The Hartle-Hawking vacuum state is defined by taking incoming modes to be positive frequency modes with respect to ∂_V (V is the canonical affine parameter on the past black hole horizon) and outgoing modes to be positive frequency modes with respect to ∂_U (U is the canonical affine parameter on the future black hole horizon). This vacuum state is time symmetric and represents the thermal equilibrium state of a black hole and Hawking radiation. The Unruh-Hawking vacuum state is defined by taking modes incoming from the past null infinity to be positive frequency modes with respect to ∂_t and those emanating from the past black hole horizon to be positive frequency modes with respect to ∂_U . This vacuum state is realized by the formation of a black hole via gravitational collapse. To specify the Unruh-Hawking vacuum state in the KdS spacetime, which is not asymptotically flat, we take modes incoming from the past cosmological horizon to be positive frequency modes with respect to ∂_{V_c} [22].

To express the vacuum condition for the Unruh-Hawking vacuum, we first introduce the up mode and the dn mode; the mode φ^{up} has support only in region II, and φ^{dn} has support only in region I (see the left panel of Fig. 2)³; they are defined by imposing their asymptotic forms at the past event horizon as

$$\varphi^{\text{up}}|_{\mathcal{H}_h^-} \sim \exp\left(i\frac{\omega_+}{\kappa_+} \ln(-U)\right) \Theta(-U), \quad \varphi^{\text{dn}}|_{\mathcal{H}_h^-} \sim \exp\left(-i\frac{\omega_+}{\kappa_+} \ln(U)\right) \Theta(U), \quad (33)$$

where $\omega_+ = \omega - m\Omega_+ > 0$ and $\Theta(x)$ is the unit step function. Even for $\omega > 0$, there is a possibility that $\omega_+ < 0$ and positive frequency modes with $\omega > 0$ become effectively negative frequency modes. These modes are called superradiant modes, which are peculiar to the Kerr spacetime. Then, the UP mode, which is the outgoing positive frequency mode with respect to the coordinate U on the past event horizon \mathcal{H}_h^- and analytic across the future event horizon \mathcal{H}_h^+ , is defined as a linear combination of φ^{up} and φ^{dn} (for $\omega, \omega_+ > 0$):

$$\varphi_{\omega_+}^{(\text{UP1})} = \frac{1}{\sqrt{2 \sinh(\pi\omega_+/\kappa_+)}} \left(e^{\pi\omega_+/2\kappa_+} \varphi_{\omega\ell m}^{\text{up}} + e^{-\pi\omega_+/2\kappa_+} (\varphi_{-\omega\ell-m}^{\text{dn}})^* \right), \quad (34)$$

$$\varphi_{-\omega_+}^{(\text{UP2})} = \frac{1}{\sqrt{2 \sinh(\pi\omega_+/\kappa_+)}} \left(e^{\pi\omega_+/2\kappa_+} \varphi_{-\omega\ell-m}^{\text{dn}} + e^{-\pi\omega_+/2\kappa_+} (\varphi_{\omega\ell m}^{\text{up}})^* \right). \quad (35)$$

The IN mode, which is the incoming positive frequency mode with respect to the coordinate V_c on the past cosmological horizon \mathcal{H}_c^- and analytic across the future cosmological horizon \mathcal{H}_c^+ , is defined as

$$\varphi_{\omega_c}^{(\text{IN1})} = \frac{1}{\sqrt{2 \sinh(\pi\omega_c/\kappa_c)}} \left(e^{\pi\omega_c/2\kappa_c} \varphi_{\omega}^{\text{in}} + e^{-\pi\omega_c/2\kappa_c} (\varphi_{-\omega}^{\text{ot}})^* \right), \quad (36)$$

$$\varphi_{-\omega_c}^{(\text{IN2})} = \frac{1}{\sqrt{2 \sinh(\pi\omega_c/\kappa_c)}} \left(e^{\pi\omega_c/2\kappa_c} \varphi_{-\omega}^{\text{ot}} + e^{-\pi\omega_c/2\kappa_c} (\varphi_{\omega}^{\text{in}})^* \right), \quad (37)$$

with $\omega_c := \omega - m\Omega_c$. The mode $\varphi_{\omega}^{\text{in}}$ has support only in the region II, $\varphi_{-\omega}^{\text{ot}}$ has support only in region III, and their asymptotic forms at the past cosmological horizon are specified by

$$\varphi^{\text{in}}|_{\mathcal{H}_c^-} \sim \exp\left(-i\frac{\omega_c}{\kappa_c} \ln(-V_c)\right) \Theta(-V_c), \quad \varphi^{\text{ot}}|_{\mathcal{H}_c^-} \sim \exp\left(i\frac{\omega_c}{\kappa_c} \ln(V_c)\right) \Theta(V_c). \quad (38)$$

The asymptotic behaviors of radial functions $R_{\omega\ell m}^{\text{in}} = \sqrt{r^2 + a^2} \varphi_{\omega\ell m}^{\text{in}}$ and $R_{\omega\ell m}^{\text{up}} = \sqrt{r^2 + a^2} \varphi_{\omega\ell m}^{\text{up}}$ are

$$R_{\omega\ell m}^{\text{up}} \rightarrow \begin{cases} e^{i\omega_+ r_*} + \tilde{\mathcal{R}}_{\omega\ell m} e^{-i\omega_+ r_*}, & r_* \rightarrow -\infty \ (r \rightarrow r_+) \\ \tilde{\mathcal{T}}_{\omega\ell m} e^{i\omega_c r_*}, & r_* \rightarrow +\infty \ (r \rightarrow r_c) \end{cases}, \quad (39)$$

$$R_{\omega\ell m}^{\text{in}} \rightarrow \begin{cases} \mathcal{T}_{\omega\ell m} e^{-i\omega_+ r_*}, & r_* \rightarrow -\infty \ (r \rightarrow r_+) \\ e^{-i\omega_c r_*} + \mathcal{R}_{\omega\ell m} e^{i\omega_c r_*}, & r_* \rightarrow +\infty \ (r \rightarrow r_c) \end{cases}, \quad (40)$$

³ The modes of the wave equation are normalized with respect to the inner product

$$(\varphi^1, \varphi^2) := i \int_{\Sigma} d\sigma^{\mu} ((\varphi^1)^* \partial_{\mu} \varphi^2 - \varphi^2 \partial_{\mu} (\varphi^1)^*),$$

where Σ is a spacelike or null hypersurface and $d\sigma^{\mu}$ is the volume element on this surface.

where reflection coefficients $\mathcal{R}_{\omega\ell m}$ and $\tilde{\mathcal{R}}_{\omega\ell m}$, and transmission coefficients $\mathcal{T}_{\omega\ell m}$ and $\tilde{\mathcal{T}}_{\omega\ell m}$ are introduced. These coefficients satisfy the following relation, which is originated from the conservation of the Wronskian:

$$1 - |\mathcal{R}_{\omega\ell m}|^2 = \frac{\omega_+}{\omega_c} |\mathcal{T}_{\omega\ell m}|^2, \quad 1 - |\tilde{\mathcal{R}}_{\omega\ell m}|^2 = \frac{\omega_c}{\omega_+} |\tilde{\mathcal{T}}_{\omega\ell m}|^2, \quad (41)$$

$$\omega_c \tilde{\mathcal{T}}_{\omega\ell m}^* \mathcal{R}_{\omega\ell m} = -\omega_+ \mathcal{T}_{\omega\ell m} \tilde{\mathcal{R}}_{\omega\ell m}^*, \quad \omega_c \tilde{\mathcal{T}}_{\omega\ell m} = \omega_+ \mathcal{T}_{\omega\ell m}. \quad (42)$$

B. Correlation function

The introduced combinations of modes $\varphi^{(\text{UP})}$ and $\varphi^{(\text{IN})}$ are called the Unruh modes. UP mode is defined on \mathcal{H}^- and IN mode is defined on \mathcal{I}^- ; Thus $\mathcal{H}^- \cup \mathcal{I}^-$ is the initial Cauchy surface to define the Unruh-Hawking vacuum state. Using the Unruh mode functions, the field operator is expanded as

$$\begin{aligned} \hat{\Phi}(x) = & \sum_{\ell m} \int_0^\infty d\omega_+ \left(\hat{a}_{\omega_+}^{(\text{UP1})} \varphi_{\omega_+}^{(\text{UP1})} + \hat{a}_{-\omega_+}^{(\text{UP2})} \varphi_{-\omega_+}^{(\text{UP2})} \right) \\ & + \sum_{\ell m} \int_0^\infty d\omega_c \left(\hat{a}_{\omega_c}^{(\text{IN1})} \varphi_{\omega_c}^{(\text{IN1})} + \hat{a}_{-\omega_c}^{(\text{IN2})} \varphi_{-\omega_c}^{(\text{IN2})} \right) + (\text{h.c.}). \end{aligned} \quad (43)$$

The Unruh-Hawking vacuum state $|U\rangle$ is defined by [22]

$$\hat{a}_{\omega_+}^{(\text{UP1})} |U\rangle = \hat{a}_{-\omega_+}^{(\text{UP2})} |U\rangle = \hat{a}_{\omega_c}^{(\text{IN1})} |U\rangle = \hat{a}_{-\omega_c}^{(\text{IN2})} |U\rangle = 0, \quad \omega_+, \omega_c \geq 0. \quad (44)$$

This state is realized by black hole formation via gravitational collapse in the KdS spacetime, and the UP and IN modes are thermally populated at the past black hole horizon and the past cosmological horizon, respectively. These modes are regular on \mathcal{H}_h^- and \mathcal{H}_c^- . The Hadamard's elementary function with the Unruh-Hawking vacuum state is (we assume $x_1, x_2 \in$ region II in Fig. 2) ⁴

$$\begin{aligned} G(x_1, x_2) & := \langle U | \{ \hat{\Phi}(x_1), \hat{\Phi}(x_2) \} | U \rangle \\ & = \sum_{\ell m} \int_0^\infty d\omega_+ \coth\left(\frac{\pi\omega_+}{\kappa_+}\right) \varphi_{\omega\ell m}^{\text{up}}(x_1) \varphi_{\omega\ell m}^{\text{up}*}(x_2) S_{\omega\ell m}(\xi_1) S_{\omega\ell m}(\xi_2) e^{im(\phi_1 - \phi_2)} \\ & \quad + \sum_{\ell m} \int_0^\infty d\omega_c \coth\left(\frac{\pi\omega_c}{\kappa_c}\right) \varphi_{\omega\ell m}^{\text{in}}(x_1) \varphi_{\omega\ell m}^{\text{in}*}(x_2) S_{\omega\ell m}(\xi_1) S_{\omega\ell m}(\xi_2) e^{im(\phi_1 - \phi_2)} + (x_1 \leftrightarrow x_2) + (\text{h.c.}) \\ & = \frac{1}{4\pi(r_1^2 + a^2)^{1/2}(r_2^2 + a^2)^{1/2}} \times \\ & \quad \sum_{\ell m} \int_0^\infty d\omega e^{-i\omega(t_1 - t_2)} \left[\frac{\Theta(\omega_+)}{\omega_+} \coth\left(\frac{\pi\omega_+}{\kappa_+}\right) R_{\omega\ell m}^{\text{up}}(r_1) R_{\omega\ell m}^{\text{up}*}(r_2) \right. \\ & \quad \left. + \frac{\Theta(\omega_c)}{\omega_c} \coth\left(\frac{\pi\omega_c}{\kappa_c}\right) R_{\omega\ell m}^{\text{in}}(r_1) R_{\omega\ell m}^{\text{in}*}(r_2) \right] S_{\omega\ell m}(\xi_1) S_{\omega\ell m}(\xi_2) e^{im(\phi_1 - \phi_2)} + (1 \leftrightarrow 2) + (\text{h.c.}), \end{aligned} \quad (45)$$

⁴ $(u_\omega(r))^* = u_{-\omega}(r)$.

where $\xi_{1,2} = \cos \theta_{1,2}$. To derive the last expression of Eq. (45), we have changed the integration variable from ω_+, ω_c to ω and introduced the unit step function in the integrand. For $r_1 = r_2 \rightarrow r_c$, the temporal Fourier component of the correlation function is given by

$$\begin{aligned}
G(\omega, \mathbf{x}_1, \mathbf{x}_2) &\propto \sum_{\ell m} \left[\frac{\Theta(\omega_+)}{\omega_+} \coth\left(\frac{\pi\omega_+}{\kappa_+}\right) |\tilde{\mathcal{T}}_{\omega\ell m}|^2 \right. \\
&\quad \left. + \frac{\Theta(\omega_c)}{\omega_c} \coth\left(\frac{\pi\omega_c}{\kappa_c}\right) |1 + \mathcal{R}_{\omega\ell m} e^{i\delta}|^2 \right] S_{\omega\ell m}(\xi_1) S_{\omega\ell m}(\xi_2) e^{im(\phi_1 - \phi_2)} \\
&\equiv G_1 + G_2,
\end{aligned} \tag{46}$$

where a phase factor $\delta = 2\omega_c r_*$ is introduced. As the radial function R^{in} is a linear combination of the incoming wave and the reflected wave with amplitude $\mathcal{R}_{\omega\ell m}$, G_2 contains phase information determined by the reflection coefficient and δ . Coefficients $\coth(\pi\omega_+/\kappa_+)$ and $\coth(\pi\omega_c/\kappa_c)$ reflect the thermal property of the black hole horizon and the cosmological horizon, respectively. For $\omega_+ \rightarrow 0$, $|\tilde{\mathcal{T}}_{\omega\ell m}| \rightarrow \omega_+$ (see Eq. (42)) and $G_1(\omega)$ is finite, whereas G_2 diverges for $\omega_c \rightarrow 0$.

The Fourier component of Hadamard's elementary function G consists of the contribution G_1 of the UP mode and G_2 of the IN mode. G_1 represents the illumination of the black hole by both the thermally populated UP mode with the Hawking temperature $\kappa_+/(2\pi)$ and vacuum fluctuation from the inside of the photon sphere. On the other hand, G_2 is the contribution of the IN mode and represents scattering of the incoming thermal radiation with temperature $\kappa_c/(2\pi)$ from the cosmological horizon and the vacuum fluctuation by the black hole. These types of radiations illuminates the black hole from the outside of the photon sphere. Concerning the superradiant phenomena, G_1 includes no superradiant modes, because it only contains $\omega_+ > 0$ modes, whereas G_2 includes superradiant modes $\omega_+ < 0 < \omega_c$ and can potentially show the superradiant scattering effect.

In G_2 , the phase factor originating from the reflection coefficient $\mathcal{R}_{\omega\ell m} e^{i\delta}$ provides the interference term between incoming and reflected waves. As the behavior of the interference term depends on r_* , and for the purpose of qualitative understanding of images of the black hole, it is convenient to evaluate G_2 by replacing $|1 + \mathcal{R}_{\omega\ell m} e^{i\delta}|^2$ with $1 + |\mathcal{R}_{\omega\ell m}|^2$, which corresponds to the dropping of the interference term between the incoming and the reflected waves by hand. For this purpose, we introduce the correlation function without the interference term as

$$\tilde{G}_2 := \sum_{\ell m} \frac{\Theta(\omega_c)}{\omega_c} \coth\left(\frac{\pi\omega_c}{\kappa_c}\right) \left(2 - \frac{\omega_c}{\omega_+} |\tilde{\mathcal{T}}_{\omega\ell m}|^2\right) S_{\omega\ell m}(\xi_1) S_{\omega\ell m}(\xi_2) e^{im(\phi_1 - \phi_2)}, \tag{47}$$

where we used the relations (41) and (42) to express $|\mathcal{R}_{\omega\ell m}|^2$ using $|\tilde{\mathcal{T}}_{\omega\ell m}|^2$. The correlation function $G = G_1 + \tilde{G}_2$ neglects the interference term between incoming and reflected waves. In the eikonal limit, as wave optical images obtained using \tilde{G}_2 correspond to images obtained by the ray tracing method in geometric optics, it is possible to identify wave effect in images by comparing images with G_2 and those with \tilde{G}_2 .

To extract the pure thermal effect of Hawking radiation, we express $G(\omega)$ for the Boulware vacuum, which includes no thermal emission from the black hole horizon and the cosmological horizons. The form of the correlation function for this vacuum state formally obtained

by taking the limits of $\kappa_+ \rightarrow 0$ and $\kappa_c \rightarrow 0$ in (46):

$$\begin{aligned}
& G^{\text{Boulware}}(\omega) \\
& \propto \sum_{\ell m} \left[\frac{\Theta(\omega_+)}{\omega_+} |\tilde{\mathcal{T}}_{\omega \ell m}|^2 + \frac{\Theta(\omega_c)}{\omega_c} |1 + \mathcal{R}_{\omega \ell m} e^{i\delta}|^2 \right] S_{\omega \ell m}(\xi_1) S_{\omega \ell m}(\xi_2) e^{im(\phi_1 - \phi_2)} \\
& = \sum_{\ell m} \left[\frac{\Theta(\omega_+)}{\omega_c} (2 + 2\text{Re}[\mathcal{R}_{\omega \ell m} e^{i\delta}]) + \frac{\Theta(-\omega_+)}{\omega_c} |1 + \mathcal{R}_{\omega \ell m} e^{i\delta}|^2 \right] S_{\omega \ell m}(\xi_1) S_{\omega \ell m}(\xi_2) e^{im(\phi_1 - \phi_2)},
\end{aligned} \tag{48}$$

where we assume that there are no superradiant modes associated with the cosmological horizon ($\omega_c > 0$). The contribution of particle creations from the black hole and the cosmological horizon in the correlation function is encoded in the following two point functions obtained by subtracting the contribution of the Boulware vacuum, and this correlation function includes the Planckian factor:

$$\begin{aligned}
& G(\omega) - G^{\text{Boulware}}(\omega) \propto \\
& \sum_{\ell m} \left[\frac{\Theta(\omega_+)}{e^{2\pi\omega_+/\kappa_+} - 1} \frac{|\tilde{\mathcal{T}}_{\omega \ell m}|^2}{\omega_+} + \frac{\Theta(\omega_c)}{e^{2\pi\omega_c/\kappa_c} - 1} \frac{|1 + \mathcal{R}_{\omega \ell m} e^{i\delta}|^2}{\omega_c} \right] S_{\omega \ell m}(\xi_1) S_{\omega \ell m}(\xi_2) e^{im(\phi_1 - \phi_2)}.
\end{aligned} \tag{49}$$

By definition, $G - G^{\text{Boulware}}$ becomes zero for $\kappa_+, \kappa_c \rightarrow 0$. We use this correlation function for images of the black hole that directly reflect the Hawking effect.

IV. EVALUATION OF TRANSMISSION AND REFLECTION COEFFICIENTS

In this section, we introduce our computation of the greybody factor $|\tilde{\mathcal{T}}_{\omega\ell m}|^2$ and the reflection coefficient $\mathcal{R}_{\omega\ell m}$. We adopt the method developed in [34], which utilizes the local solutions around regular singular points of the Heun equation (local Heun function) with the Frobenius method to construct solutions of the Teukolsky equation. The local Heun functions have been implemented as built-in functions in Mathematica version 12.1 released in 2020. Here, we discuss the relation between scattering problems based on the Teukolsky radial function $R^{(T)}$ and on the radial function R introduced in (26). They are related as $R^{(T)} = R/\sqrt{r^2 + a^2}$. $R^{(T)}$ obeys

$$\left[\frac{d}{dr} \Delta_r \frac{d}{dr} + \frac{\chi^4}{\Delta_r} [\omega(r^2 + a^2) - am]^2 - \frac{2\Lambda}{3} r^2 - \lambda_{\ell m}(a\omega, \Lambda) \right] R^{(T)} = 0. \quad (50)$$

This equation is the same as that of the massless conformal scalar field in the KdS spacetime. To use the method with the local Heun function, we transform the above equation into the Heun equation by introducing the coordinate transformation from r to z and the redefinition of the radial equation:

$$z = \frac{r_c - r_-}{r_c - r_+} \frac{r - r_+}{r - r_-}, \quad R^{(T)} = z^{B_1} (z - 1)^{B_2} (z - z_r)^{B_3} (z - z_\infty) y^{(r)}(z), \quad (51)$$

and the radial equation yields

$$\frac{d^2 y^{(r)}}{dz^2} + \left(\frac{2B_1 + 1}{z} + \frac{2B_2 + 1}{z - 1} + \frac{2B_3 + 1}{z - z_r} \right) \frac{dy^{(r)}}{dz} + \frac{(1 - 2B_4)z + v}{z(z - 1)(z - z_r)} y^{(r)} = 0, \quad (52)$$

where

$$z_\infty = \frac{r_c - r_-}{r_c - r_+}, \quad z_r = z_\infty \frac{r_{--} - r_+}{r_{--} - r_-}, \quad B_j = i \frac{\chi^2 (r_j^2 + a^2) (\omega - m\Omega_j)}{\Delta'_r(r_j)}, \quad (53)$$

with $B_1 = B_+$, $B_2 = B_c$, $B_3 = B_{--}$, $B_4 = B_-$, and

$$v = \frac{\lambda_{\ell m} - (\Lambda/3)(r_+ r_- + r_c r_{--})}{(\Lambda/3)(r_- - r_{--})(r_+ - r_c)} - \frac{i[2\chi^2\{\omega(r_+ r_- + a^2) - am\}]}{(\Lambda/3)(r_- - r_{--})(r_- - r_+)(r_+ - r_c)}. \quad (54)$$

The sets of the linear independent local solutions of Eq. (52) at $z = 0$ (black hole outer horizon) and at $z = 1$ (cosmological horizon) are represented as (y_{01}, y_{02}) and (y_{11}, y_{12}) , respectively [34]. These solutions are related to each other as

$$y_{01}(z) = C_{11} y_{11}(z) + C_{12} y_{12}(z), \quad y_{02}(z) = C_{21} y_{11}(z) + C_{22} y_{12}(z), \quad (55)$$

$$y_{11}(z) = D_{11} y_{01}(z) + D_{12} y_{02}(z), \quad y_{12}(z) = D_{21} y_{01}(z) + D_{22} y_{02}(z), \quad (56)$$

with the connection coefficients

$$C_{11} = \frac{W_z[y_{01}, y_{12}]}{W_z[y_{11}, y_{12}]}, \quad C_{12} = \frac{W_z[y_{01}, y_{11}]}{W_z[y_{12}, y_{11}]}, \quad C_{21} = \frac{W_z[y_{02}, y_{12}]}{W_z[y_{11}, y_{12}]}, \quad C_{22} = \frac{W_z[y_{02}, y_{11}]}{W_z[y_{12}, y_{11}]}, \quad (57)$$

and

$$D_{11} = \frac{W_z[y_{11}, y_{02}]}{W_z[y_{01}, y_{02}]}, \quad D_{12} = \frac{W_z[y_{11}, y_{01}]}{W_z[y_{02}, y_{01}]}, \quad D_{21} = \frac{W_z[y_{12}, y_{02}]}{W_z[y_{01}, y_{02}]}, \quad D_{22} = \frac{W_z[y_{12}, y_{01}]}{W_z[y_{02}, y_{01}]}, \quad (58)$$

where $W_z[u, v] = u(dv/dz) - v(du/dz)$. Note that the local solutions are evaluated with the built-in function `HeunG` in `Mathematica`⁵.

To obtain the greybody factor and reflection coefficient, we investigate the behavior of the in and up modes in terms of $R(r_*)$ and $R^T(r)$. In the tortoise coordinate r_* , the up and in modes have been obtained as Eqs. (39) and (40), respectively. Equivalently, in the r coordinate, it is expressed as

$$R^{(T)\text{up}} \rightarrow \begin{cases} D^{(\text{up})} \Delta_r^{B_1} + D^{(\text{ref})} \Delta_r^{-B_1}, & r \rightarrow r_+ \\ D^{(\text{trans})} \Delta_r^{B_2}, & r \rightarrow r_c \end{cases} \quad (59)$$

$$R^{(T)\text{in}} \rightarrow \begin{cases} C^{(\text{trans})} \Delta_r^{-B_1}, & r \rightarrow r_+ \\ C^{(\text{ref})} \Delta_r^{B_2} + C^{(\text{inc})} \Delta_r^{-B_2}, & r \rightarrow r_c. \end{cases} \quad (60)$$

The reflection coefficient $\mathcal{R}_{\omega\ell m}$ and the greybody factor $|\tilde{\mathcal{G}}_{\omega\ell m}|^2$ can be written with the coefficients of the above solutions as

$$\mathcal{R}_{\omega\ell m} = \frac{C^{(\text{ref})}}{C^{(\text{inc})}}, \quad |\tilde{\mathcal{G}}_{\omega\ell m}|^2 = \left(\frac{r_c^2 + a^2}{r_+^2 + a^2} \right) \left| \frac{D^{(\text{trans})}}{D^{(\text{up})}} \right|^2 \quad (61)$$

by comparing the asymptotic form of $R(r_*)$ and $R^T(r)$ using the relation between r_* and r . Furthermore, $C^{(\text{ref/up/trans})}$ and $D^{(\text{ref/up/trans})}$ are represented with the connection coefficients of the local Heun functions as demonstrated in [34] as

$$C^{(\text{inc})} = C_{22}(-1)^{B_2}(1-z_r)^{B_3}(1-z_\infty)(A_2)^{-B_2}, \quad (62)$$

$$\begin{aligned} C^{(\text{ref})} &= C_{21}D^{(\text{trans})} \\ &= C_{21}(-1)^{B_2}(1-z_r)^{B_3}(1-z_\infty)(A_2)^{B_2}, \end{aligned} \quad (63)$$

$$D^{(\text{up})} = D_{11}(-1)^{B_2}(-z_r)^{B_3}(-z_\infty)(A_1)^{B_1}, \quad (64)$$

$$\begin{aligned} D^{(\text{ref})} &= D_{12}C^{(\text{trans})} \\ &= D_{12}(-1)^{B_2}(-z_r)^{B_3}(-z_\infty)(A_1)^{-B_1}, \end{aligned} \quad (65)$$

with

$$A_1 = \frac{z_\infty}{(r_+ - r_-)\Delta'(r_+)}, \quad A_2 = \frac{z_\infty(r_+ - r_-)}{-(r_c - r_-)^2\Delta'(r_c)}. \quad (66)$$

⁵ See the detailed computation in [34].

V. IMAGING OF BLACK HOLES WITH HAWKING RADIATION

As we have shown in Eq. (18), the qubit detector system is applicable to the detection of the spatial correlation of Hawking radiation, and we adopt it as our imaging system for black holes.

A. Detail of imaging method and an example with a simple model

In our imaging setup, two detectors are placed near the cosmological horizon. In the spherical coordinate system, detector 1 is placed at $(r, \theta_1, \phi_1) = (r, \pi/2, 0)$ (on the equatorial plane), and detector 2 is placed at (r, θ_2, ϕ_2) . In the Cartesian coordinates $(x, y, z) = (r \sin \theta \cos \phi, r \sin \theta \sin \phi, r \cos \theta)$, the detector locations are

$$\mathbf{x}_1 = (r, 0, 0), \quad \mathbf{x}_2 = (r \sin \theta \cos \phi, r \sin \theta \sin \phi, r \cos \theta). \quad (67)$$

We define two-dimensional coordinates in the observer's screen as

$$\mathbf{X} = (X, Y) = (\sin \theta \sin \phi, \cos \theta). \quad (68)$$

Then, the locations of two detectors in the observer's screen are

$$(X_1, Y_1) = (0, 0) = \mathbf{X}_1, \quad (X_2, Y_2) = (\sin \theta \sin \phi, \cos \theta) = \mathbf{X}_2. \quad (69)$$

Applying Eq. (10), images (intensity distributions) are obtained through the following Fourier transformation of the correlation function in the observer's screen:

$$\mathcal{F}[G](\mathbf{X}_{\text{im}}) := \int d^2 \mathbf{X}_{12} G(\omega, \mathbf{X}_1, \mathbf{X}_2) \exp(i\omega \mathbf{X}_{\text{im}} \cdot \mathbf{X}_{12}), \quad \mathbf{X}_{12} = \mathbf{X}_1 - \mathbf{X}_2, \quad (70)$$

where \mathbf{X}_{im} denotes coordinates in the image plane.

To check our imaging method, we analytically evaluate images for the model correlation function $G = G_1 + \tilde{G}_2$, which includes important features of the correlation function of Hawking radiation from the Schwarzschild-de Sitter black hole:

$$G_1 = \frac{g_1}{\omega} \sum_{\ell=0}^{\infty} \Theta(\ell_* - \ell) (2\ell + 1) P_\ell(\cos \Delta), \quad \tilde{G}_2 = \frac{g_2}{\omega} \sum_{\ell=0}^{\infty} (1 + \Theta(\ell - \ell_*)) (2\ell + 1) P_\ell(\cos \Delta). \quad (71)$$

Here, P_ℓ is the Legendre polynomial. The transmission and reflection coefficients are replaced with the unit step function to reflect the property of perfect absorption of black holes. The parameter ℓ_* denotes the critical angular momentum of perfect absorption corresponding to the photon sphere, and $\Delta := \theta - \pi/2$ is the angle between an observing point and the optical axis. In the eikonal limit, the critical impact parameter of photons is ℓ_*/ω which corresponds to the size of the black hole shadow. This model well represents the correlation function of Hawking radiation in the eikonal region. The constants g_1 and g_2 depend on the surface gravity of horizons

$$g_1 = \coth\left(\frac{\pi\omega}{\kappa_+}\right), \quad g_2 = \coth\left(\frac{\pi\omega}{\kappa_c}\right). \quad (72)$$

By replacing the sum with an integral, it is possible to evaluate the correlation function analytically; with the approximation $P_\ell(\cos \Delta) \sim J_0(\ell\Delta)$, $\ell \gg 1$ and by replacing the upper bound of the infinite sum by $\ell_{\max} \gg \ell_*$, we obtain

$$G_1 \approx \frac{2g_1}{\omega} \int_0^{\ell_*} d\lambda \lambda P_\lambda(\cos \Delta) = \frac{2g_1}{\omega} \int_0^{\ell_*} d\lambda \lambda J_0(\lambda\Delta) = \frac{2g_1 \ell_*}{\omega \Delta} J_1(\ell_* \Delta), \quad (73)$$

where J_0 and J_1 are Bessel functions and

$$\begin{aligned} \tilde{G}_2 &= \frac{g_2}{\omega} \sum_{\ell=0}^{\ell_{\max}} (2\ell + 1) P_\ell(\cos \Delta) + \frac{g_2}{\omega} \left(\sum_{\ell=0}^{\ell_{\max}} - \sum_{\ell=0}^{\ell_*} \right) (2\ell + 1) P_\ell(\cos \Delta) \\ &\approx \frac{4g_2}{\omega} \frac{\ell_{\max}}{\Delta} J_1(\ell_{\max} \Delta) - \frac{2g_2 \ell_*}{\omega \Delta} J_1(\ell_* \Delta). \end{aligned} \quad (74)$$

The angle Δ is related to the coordinates (X, Y) in the observer's screen as $|\Delta| = \sqrt{X^2 + Y^2} < 1$.

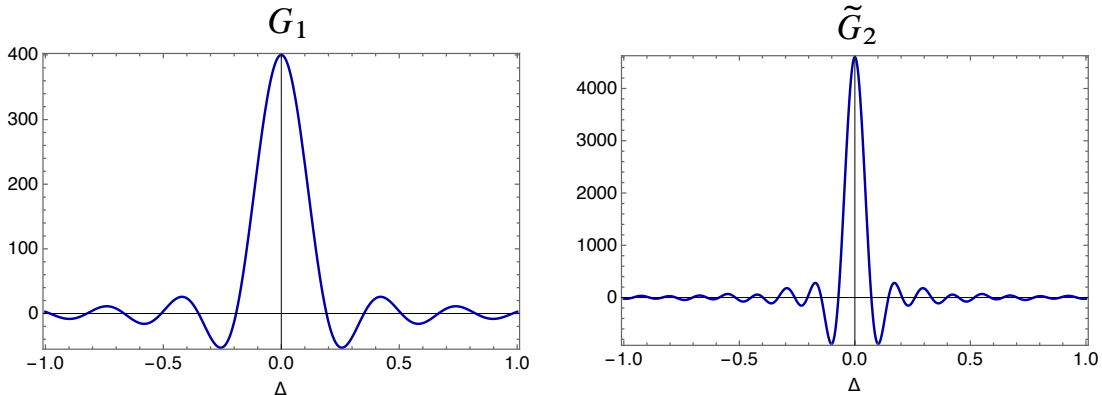


FIG. 3: G_1 and \tilde{G}_2 with $\ell_* = 20$, $\ell_{\max} = 50$, $\omega = 1$, and $g_1 = g_2 = 1$.

Figure 3 shows the behavior of G_1 and \tilde{G}_2 . G_1 represents the interference fringe due to Hawking radiation from the black hole. For $\ell_{\max} \rightarrow \infty$, the peak of \tilde{G}_2 at $\Delta = 0$ becomes infinite, and the peak approaches the Dirac delta function.

Now, we consider the two-dimensional Fourier transformation (70) of a function $f(\sqrt{X^2 + Y^2})$:

$$\mathcal{F}[f] = \frac{1}{2\pi} \int_{-\infty}^{+\infty} dX dY f(\sqrt{X^2 + Y^2}) e^{i\omega(X_{\text{im}}X + Y_{\text{im}}Y)}, \quad (75)$$

where X_{im} and Y_{im} are coordinates in the image plane. Then,

$$\begin{aligned} \mathcal{F}[f] &= \frac{1}{2\pi} \int_0^\infty \Delta(d\Delta) \int_0^{2\pi} d\phi f(\Delta) e^{i\omega \sqrt{X_{\text{im}}^2 + Y_{\text{im}}^2} \Delta \cos \phi} \\ &= \int_0^\infty \Delta(d\Delta) J_0(\omega R_{\text{im}} \Delta) f(\Delta), \end{aligned} \quad (76)$$

where $R_{\text{im}} := \sqrt{X_{\text{im}}^2 + Y_{\text{im}}^2}$. Applying this formula⁶, we obtain

$$\mathcal{F}[G_1] \propto \frac{2g_1}{\omega} \Theta(\ell_*/\omega - R_{\text{im}}), \quad (77)$$

$$\mathcal{F}[\tilde{G}_2] \propto \frac{4g_2}{\omega} \Theta(\ell_{\text{max}}/\omega - R_{\text{im}}) - \frac{2g_2}{\omega} \Theta(\ell_*/\omega - R_{\text{im}}), \quad (78)$$

$$\mathcal{F}[G_1 + \tilde{G}_2] \propto \frac{4g_2}{\omega} \Theta(\ell_{\text{max}}/\omega - R_{\text{im}}) - \frac{2g_2 - 2g_1}{\omega} \Theta(\ell_*/\omega - R_{\text{im}}). \quad (79)$$

Figure 4 shows images obtained from the correlation function (71).

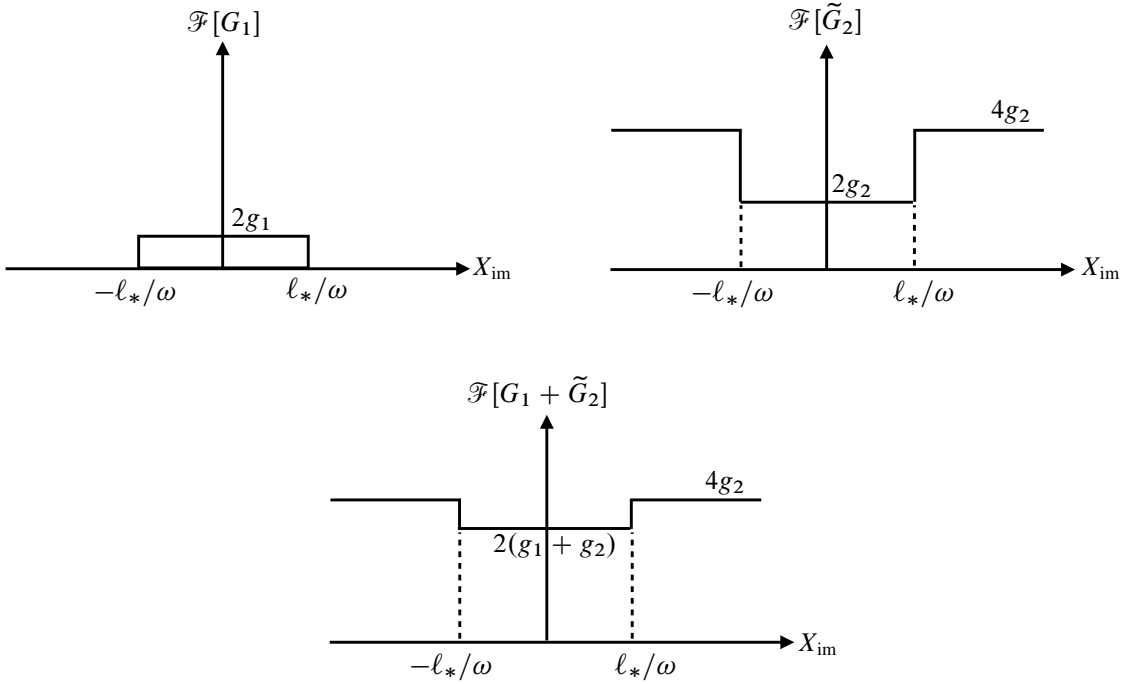


FIG. 4: One-dimensional images obtained from the correlation function (71). The lower panel is $\mathcal{F}[G_1 + \tilde{G}_2]$. The red line is for the case of $g_1 < g_2$ ($\kappa_+ < \kappa_c$) and the blue line is for the case of $g_1 > g_2$ ($\kappa_+ > \kappa_c$). For high frequency, $g_1 = g_2$, and $\mathcal{F}[G_1 + \tilde{G}_2]$ is constant.

For high frequency, $\omega > \kappa_{+,c}/(2\pi)$, and $g_1 \approx g_2 \approx 1$ holds. The image $\mathcal{F}[G_1]$ is a bright disk with the intensity $2g_1$, which represents Hawking radiation from the black hole. On the other hand, the image $\mathcal{F}[\tilde{G}_2]$ shows a dark shadow of the black hole in bright background, which is originated from emission of the cosmological horizon. $\mathcal{F}[G_1 + \tilde{G}_2]$ is constant, and the images $\mathcal{F}[G_1]$ and $\mathcal{F}[\tilde{G}_2]$ complement each other. On the other hand, for low frequency $\omega < \kappa_{+,c}/(2\pi)$, $g_1 \approx \kappa_+/(2\pi\omega)$, and $g_2 \approx \kappa_c/(2\pi\omega)$. Thus, for $\kappa_+ < \kappa_c$, emission from the cosmological horizon has a higher temperature than that of the black hole, and the image $\mathcal{F}[G_1 + \tilde{G}_2]$ shows a dark shadow with radius ℓ_*/ω . On the contrary, for $\kappa_+ > \kappa_c$, the image

⁶

$$\int_0^\infty dx J_0(ax) J_1(bx) = \frac{1}{b} \Theta(b - a).$$

$\mathcal{F}[G_1 + \tilde{G}_2]$ shows a bright disk, which represents the emission of Hawking radiation from the black hole.

B. Black hole images

Now, we proceed to image reconstruction of black holes using Eqs. (46) and (49). Assuming that detector 1 is located on the equatorial plane reduces much computational time because in the summation with respect to ℓ and m of G_1 and G_2 , the spheroidal harmonics $S_{\omega\ell m}(\pi/2, 0)$ is nonzero only for $m = \ell, \ell - 2, \dots, -(\ell - 2), -\ell$. To evaluate G_2 , we must truncate infinite sum of ℓ with a sufficiently large value ℓ_{\max} that does not change the qualitative behavior of the correlation function. A rough estimation to determine ℓ_{\max} is as follows: for the radial distance of observation r_{obs} , ℓ_{\max} is estimated as $r_{\text{obs}} \sim \ell_{\max}/\omega$. Thus, $\ell_{\max} \gtrsim \omega r_{\text{obs}}$ is required. In our calculation, we choose $\ell_{\max} = 70$ for $\omega = 5$ and $\ell_{\max} = 7$ for $\omega = 0.5$. These values are chosen to be larger than the value of ℓ corresponding to the photon sphere of the black hole. The original correlation function, Eq. (45), includes the prefactor $1/(4\pi(r_{\text{obs}}^2 + a^2))$, which depends on r_{obs} . This factor only affects the total intensity of images, and the structure of images is not altered if we omit this factor. G_2 contains r_{obs} as the phase factor $\delta = 2\omega_c r_*|_{\text{obs}}$. In our analysis, we do not fix r_{obs} , and δ is chosen as $0, \pi/2, \pi, 3\pi/2$. As the black hole parameters, we choose $a = 0, 0.1, \text{ and } 1$ as well as $\Lambda = 1/100$. For these values, the horizon radius and surface gravity are (in units of $M = 1$)

$$\begin{aligned}
a = 0 : & \quad r_+ = 2.028, \quad r_c = 16.22, \quad \kappa_+ = 0.2364, \quad \kappa_c = 0.05026, \\
a = 0.1 : & \quad r_+ = 2.023, \quad r_c = 16.22, \quad \kappa_+ = 0.2359, \quad \kappa_c = 0.05025, \\
a = 1 : & \quad r_+ = 1.094, \quad r_c = 16.22, \quad \kappa_+ = 0.03685, \quad \kappa_c = 0.05015.
\end{aligned} \tag{80}$$

In the observer's screen, we evaluate G_1 and G_2 in a region $-1 \leq \theta - \pi/2 \leq 1, -1 \leq \phi \leq 1$ with 60×60 sampling points by taking the summation with respect to ℓ and m . In our calculation of images, we pick data points of $X^2 + Y^2 < 1/4$ in the observer's screen, which defines the aperture of our imaging system. We applied the Tukey window to reduce unwanted aliasing originating from the sharp cutoff of the aperture in discrete Fourier transformation in a finite region. Around the equatorial plane $\theta \approx \pi/2$, difference between the spheroidal harmonics $S_{\omega\ell m}$ and the spherical harmonics $Y_{\ell m}$ is not so large; indeed, the relative difference between them is smaller than 0.1 even for $\ell \geq 5$ with $a\omega = 5$. Thus, we evaluate the sum in G by replacing $S_{\omega\ell m}$ with $Y_{\ell m}$ to reduce computational time. We checked that the relative difference of G is less than 1 % for $a\omega = 5$; hence, we expect that this replacement does not produce much qualitative difference in the images.

1. Images for $a = 0$ (Schwarzschild case)

Figure 5 shows the reflection and transmission coefficients in the (ℓ, m) -plane as well as G_1 and G_2 for $\omega = 5$. As the black hole is spherically symmetric, the reflection and transmission coefficients have no m dependence. The ℓ dependence of the reflection coefficient contains information of the phase shift of waves scattered by the black hole. For $\ell \leq \ell_* \approx 25$, $\mathcal{R}_{\omega\ell m} \sim 0, \tilde{\mathcal{T}}_{\omega\ell m} \sim 1$, and incoming waves from spatial infinity are perfectly absorbed by the black hole. In wave optics, the photon sphere corresponds to a boundary between perfect

absorption and perfect reflection in the (ℓ, m) -plane. In the eikonal limit, the boundary is represented as a relation between ℓ and m , which corresponds to a set of bounded photon orbits. This critical value $l_*/\omega \sim 5M$ corresponds to the size of photon sphere of the Schwarzschild black hole. $|\mathcal{R}_{\omega\ell m}|$ and $|\tilde{\mathcal{T}}_{\omega\ell m}|$ satisfy the conservation law $|\mathcal{R}_{\omega\ell m}|^2 + |\tilde{\mathcal{T}}_{\omega\ell m}|^2 = 1$. The correlation functions G_1 and G_2 on the observer's screen show circular interference fringes. G_2 has a sharp peak at the origin, which originated from the incoming radiation from the cosmological horizon. The Fourier transformation of this peak provides a nearly homogeneous background intensity of images. The imaginary part of G is zero for $a = 0$.

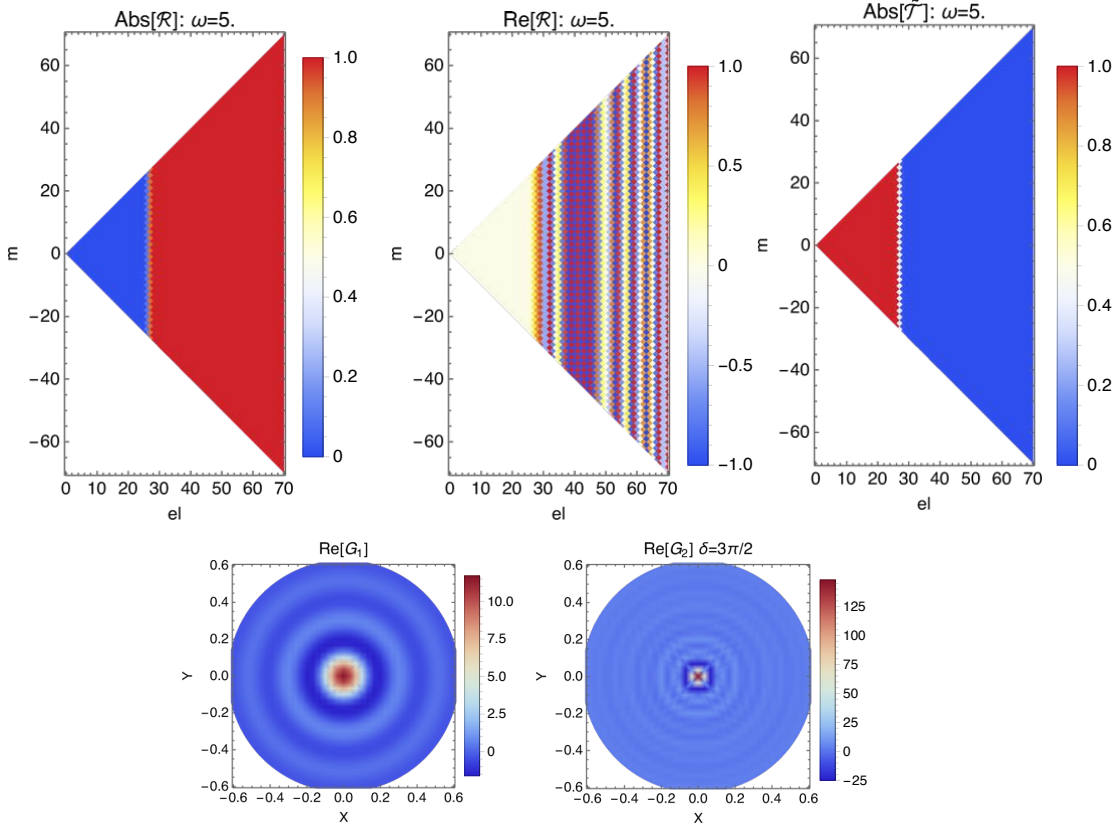


FIG. 5: Reflection and transmission coefficients in the (ℓ, m) -plane (upper panels) as well as G_1 and G_2 on the observer's screen (lower panels) for $a = 0$ with $\omega = 5$. G_1 shows interference fringes caused by Hawking radiation emitted by the black hole. G_2 shows the interference fringes caused by scattering of incoming radiation from the cosmological horizon by the black hole. A sharp peak in G_2 at $X = Y = 0$ is due to the background incoming mode from the cosmological horizon, which results in homogeneous background intensity distribution in images. The imaginary part of $G_{1,2}$ is zero.

Figure 6 shows images obtained by the Fourier transformation of G . $\mathcal{F}[G_1]$ is the image of the black hole illuminated by the UP mode with the vacuum fluctuation. We superimpose the photon sphere (dotted circle) with the image. As the photon sphere is a concept in geometric optics, its shape has a finite width in wave optics. To identify the location of the photon sphere in our calculation, we define it as the location where the intensity of $\mathcal{F}[G_1]$ becomes half of that of the central bright region. The black hole has the appearance of a “shining star” with its surface coinciding with the photon sphere. $\mathcal{F}[G_2]$ and $\mathcal{F}[\tilde{G}_2]$ are

images of the black hole illuminated by the IN mode, which is incoming radiation from the cosmological horizon. The emission from the black hole is not included in G_2 or \tilde{G}_2 . The incoming radiation is scattered and absorbed by the black hole. A dark circular shadow region surrounded by a bright ring appears in these images. The shadow region is not black, because G_2 has a contribution from incoming waves directly reaching the detectors from the cosmological horizon (see Fig. 4). $\mathcal{F}[G_1 + G_2]$ and $\mathcal{F}[G_1 + \tilde{G}_2]$ are images with contributions from both the UP mode and the IN mode. The black hole is visible as a bright disk in $\mathcal{F}[G_1 + G_2]$. A comparison of these two images reveals that the interference effect sharpens the structure of the photon sphere. We can confirm this behavior more clearly by checking one-dimensional slice of the images (right panels of Fig. 6; slices of images along the $Y_{\text{im}} = 0$ line). Depending on the values of the phase δ , the intensity around the photon sphere becomes brighter or darker than that of the image without the interference effect. The intensity inside and outside of the photon sphere is not affected by the values of δ .

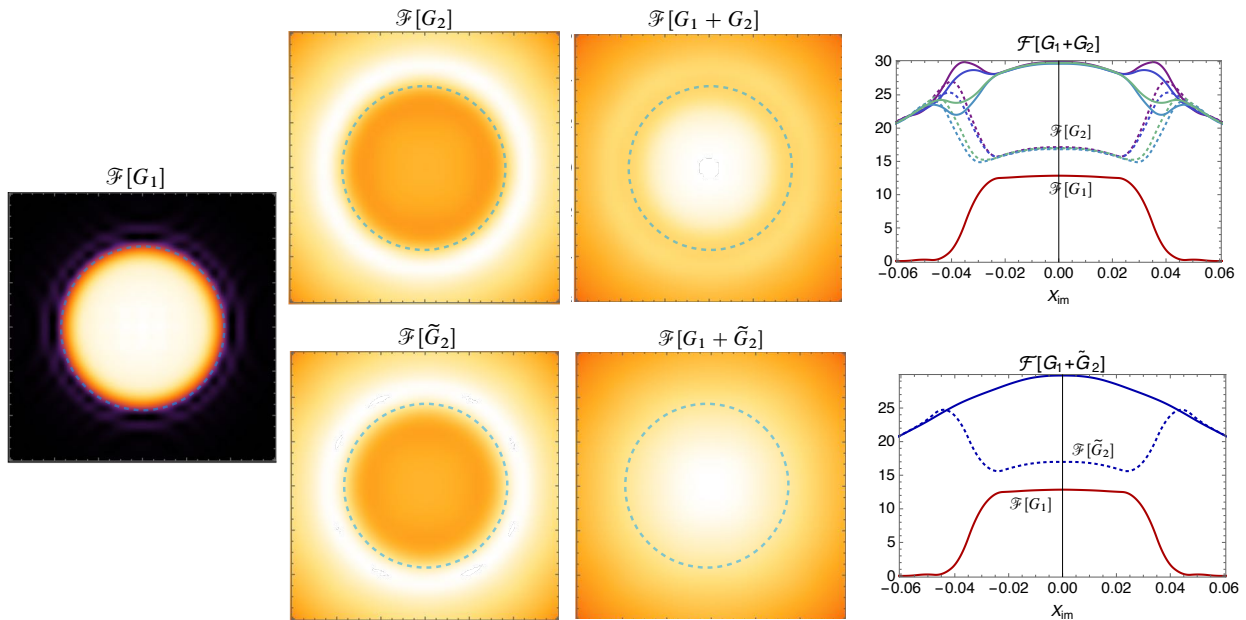


FIG. 6: Images for $a = 0$ and $\omega = 5$. Two-dimensional images with $\delta = 3\pi/2$ and one-dimensional slice of images along $Y_{\text{im}} = 0$ (right panels). Dotted circles in two-dimensional images represent the photon sphere. In the one-dimensional slice of $\mathcal{F}[G_1 + G_2]$, images with four different phases $\delta = 0, \pi/2, \pi,$ and $3\pi/2$, are shown.

Figures 7 and 8 show the results for $\omega = 0.5$. From $|\tilde{\mathcal{T}}_{\omega\ell m}|$ and $\mathcal{R}_{\omega\ell m}$, $\ell_* \approx 2$ corresponds to the location of the photon sphere, but the shape of the photon sphere becomes hazy for low frequency. The image of G_1 spreads over the field of view, and the structure of the photon sphere is not visible as an image. This is because small ℓ modes mainly contribute to G_1 for the low-frequency case. The image of G shows that the entire field of view becomes bright, and the brightness is much larger than that for $\omega = 5$ because the emission of Hawking radiation is mainly supported by the low-frequency mode $\omega \sim \kappa_+/(2\pi)$, the wavelength of which is much larger than the size of the photon sphere.

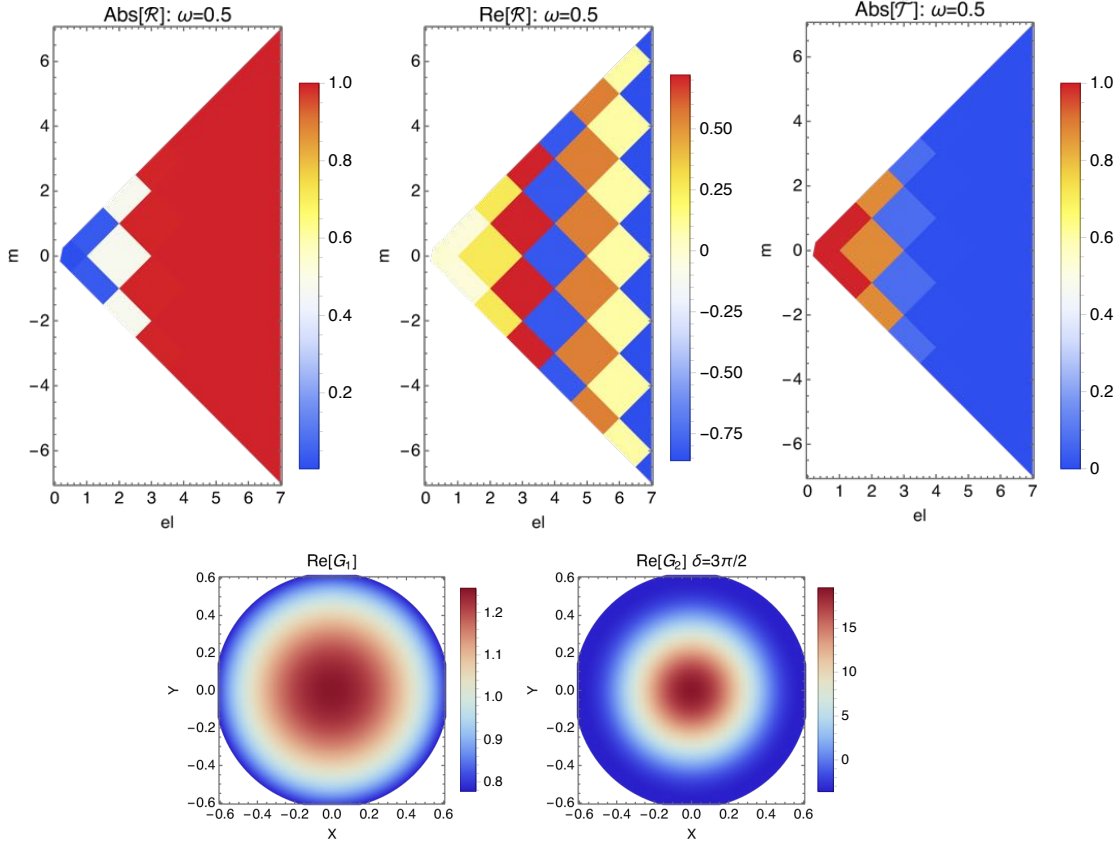


FIG. 7: Reflection and transmission coefficients in the (ℓ, m) -plane (upper panels) as well as G_1 and G_2 (lower panels) for $a = 0$ and $\omega = 0.5$. The imaginary part of $G_{1,2}$ is zero.

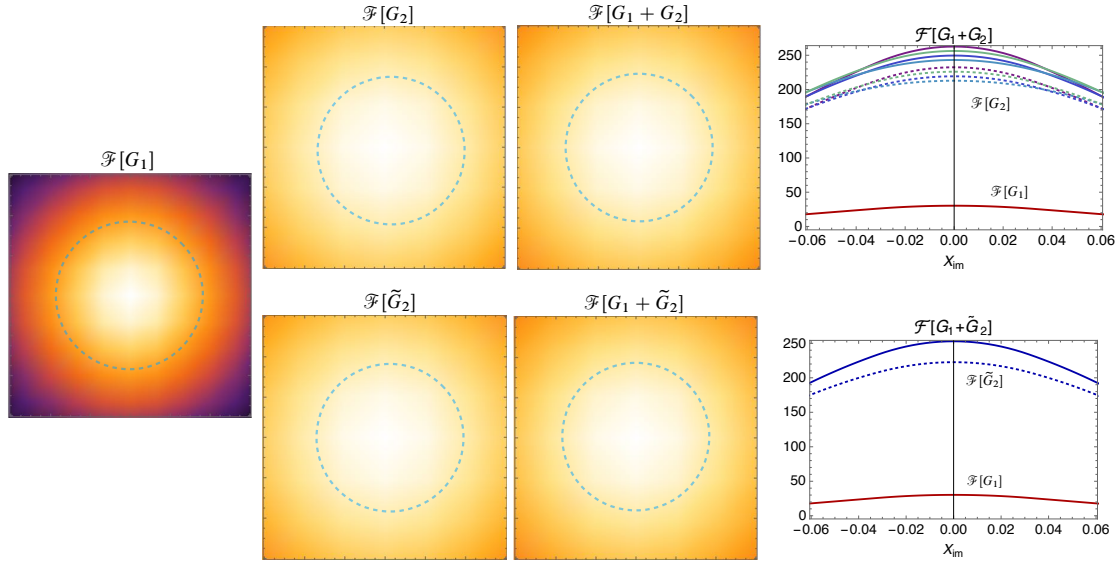


FIG. 8: Images for $a = 0$ and $\omega = 0.5$. Two-dimensional images are drawn with $\delta = 3\pi/2$. Dotted circles in two-dimensional images represent the photon sphere. The entire field of view becomes bright, and it is not possible to identify the structure of the photon sphere.

2. Images for $a = 1/10$ (slowly rotating case)

Figures 9 and 10 show the reflection and transmission coefficients as well as images for $a = 1/10$ and $\omega = 5$. The introduction of a small spin results in a small deformation of $\mathcal{R}_{\omega\ell m}$ and $\tilde{\mathcal{T}}_{\omega\ell m}$ and causes the m dependence of these coefficients. The small spin parameter leads to a nonzero imaginary part of $G_{1,2}$, which results in a left-right asymmetric fringe pattern in the observer's screen. The image of G_1 shows a spherical photon sphere, which is not possible to distinguish for the image of $a = 0$. However, the images of G_2 shows an irregular-shaped ring, which is caused by the interference effect between incoming and outgoing waves. Indeed, the image of \tilde{G}_2 shows a circular ring corresponding to the photon sphere. Moreover, the interference effect enhances the left-right asymmetry of intensity of images around the photon sphere, which is clearly visible from the one-dimensional slice of images (right panels of Fig. 10).

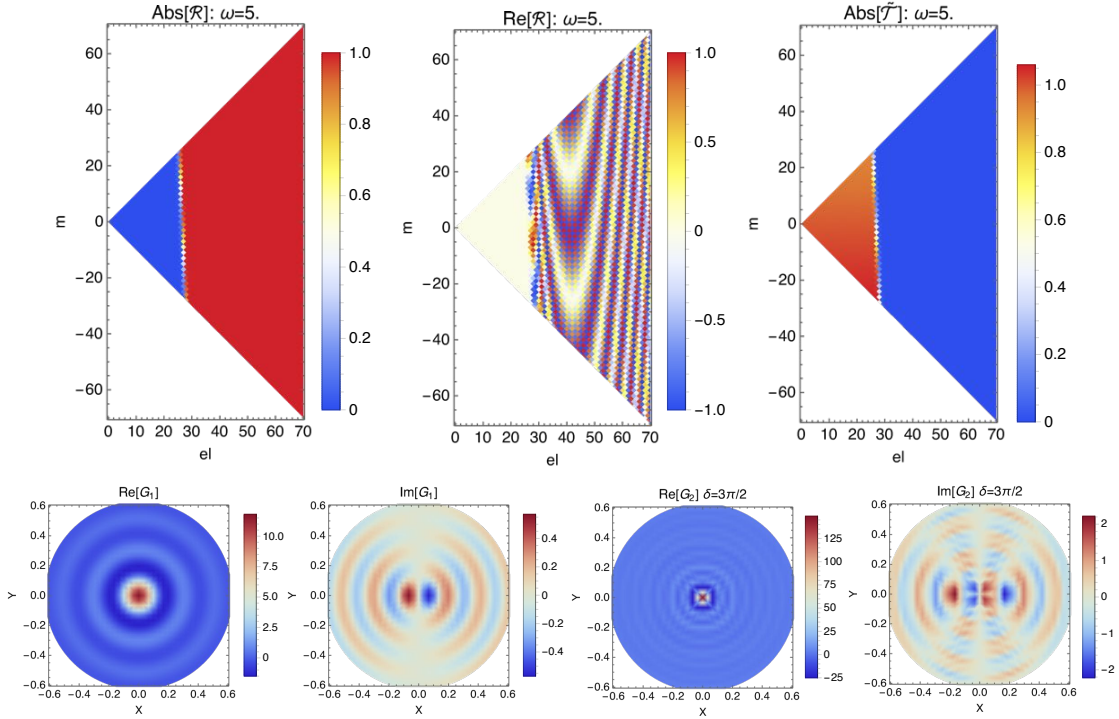


FIG. 9: Reflection and transmission coefficients in the (ℓ, m) -plane (upper panels) as well as G_1 and G_2 (lower panels) for $a = 0.1$ and $\omega = 5$. The reflection and transmission coefficients show m dependence. The imaginary part of $G_{1,2}$ presents left-right asymmetric fringe patterns, which are caused by the small value of the spin parameter.

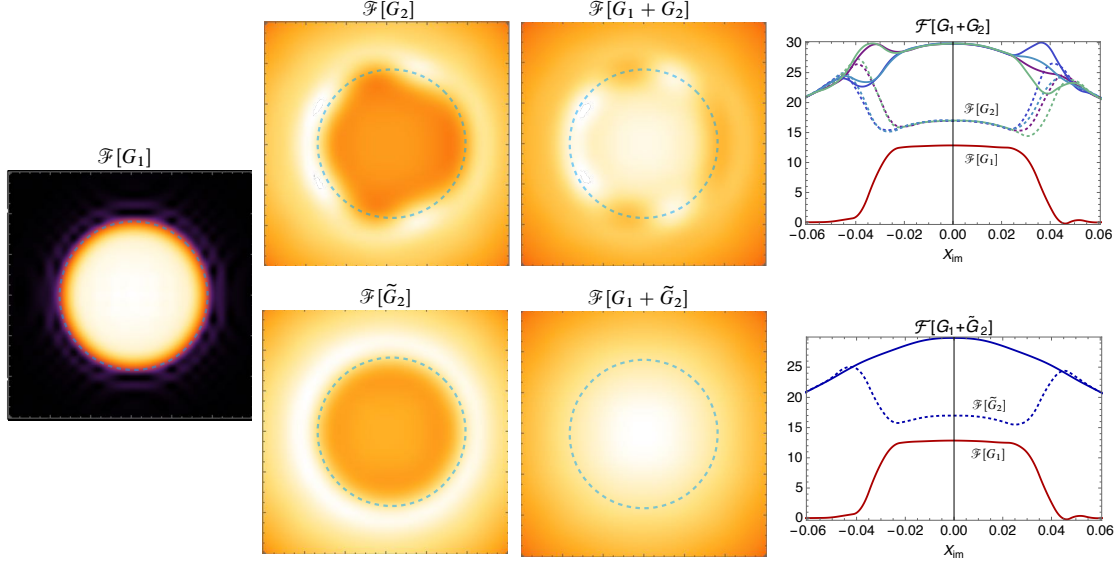


FIG. 10: Images for $a = 1/10$ and $\omega = 5$. Two-dimensional images are obtained with $\delta = 3\pi/2$. Dotted circles in the two-dimensional images represent the photon sphere. The asymmetry of $\mathcal{F}[G_2]$ and $\mathcal{F}[G_1 + G_2]$ reflect the effect of the small nonzero value of the spin parameter.

Figures 11 and 12 show the reflection and transmission coefficients as well as images for $a = 1/10$ and $\omega = 0.5$. $|\tilde{\mathcal{T}}_{\omega\ell m}|$ and $\mathcal{R}_{\omega\ell m}$ show a small m dependence. It is not possible to distinguish the ℓ dependence from that for $a = 0$ and $\omega = 0.5$. The small a induces the imaginary part of G , which shows left-right asymmetry. We cannot recognize the shape of the emission region of Hawking radiation (Fig. 12). The effect of the small spin parameter is manifested as a small left-right asymmetry in the one-dimensional intensity distribution (right panel of Fig. 12).

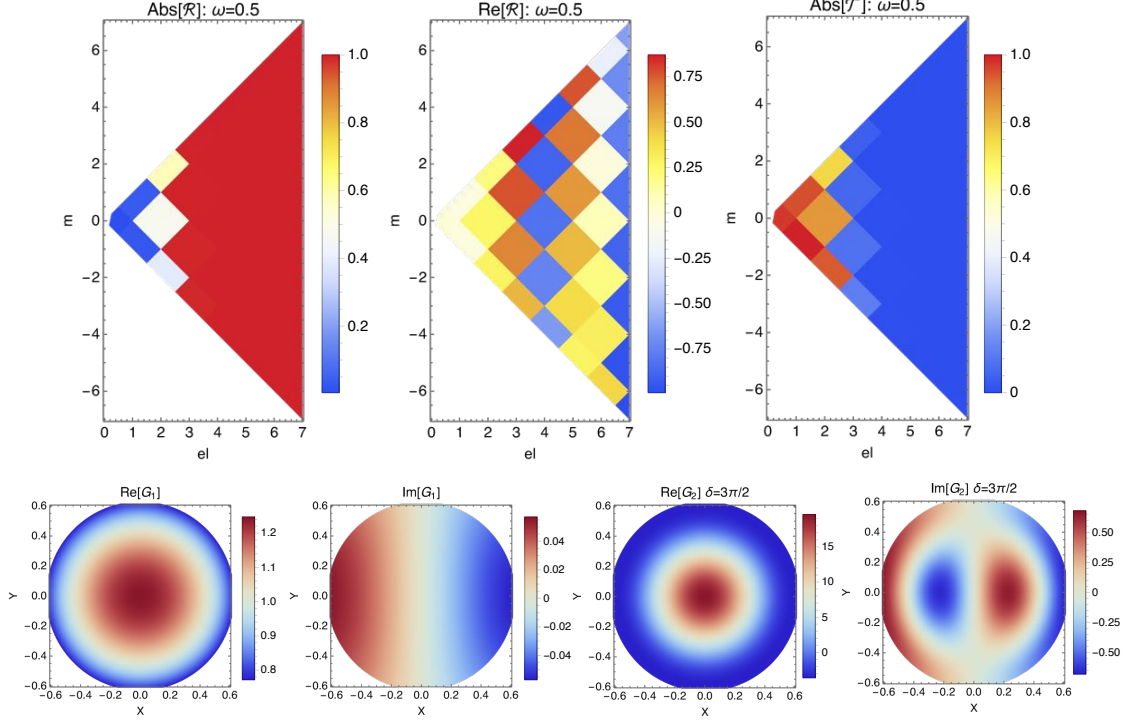


FIG. 11: Reflection and transmission coefficients in the (ℓ, m) -plane (upper panels) as well as G_1 and G_2 (lower panels) for $a = 1/10$ and $\omega = 0.5$. The left-right asymmetry of fringe patterns of $\text{Im}[G_1]$ and $\text{Im}[G_2]$ is also shown for the low-frequency case.

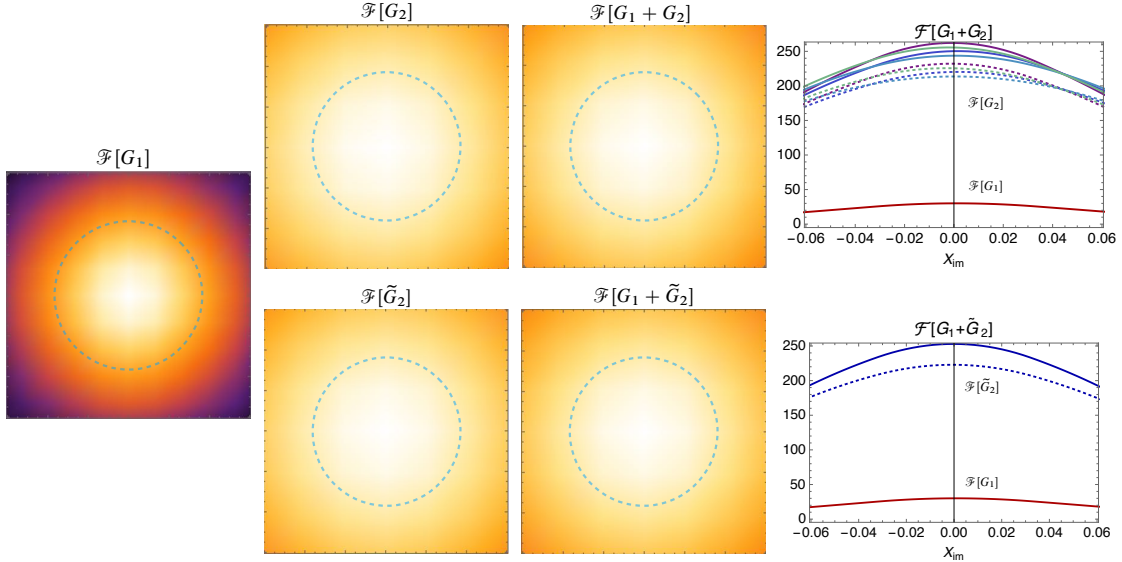


FIG. 12: Images for $a = 1/10$ and $\omega = 0.5$. Two-dimensional images are obtained with $\delta = 3\pi/2$. Dotted circles in two-dimensional images represent the photon sphere. Left-right asymmetry is visible in $\mathcal{F}[G_1 + G_2]$.

3. Images for $a = 1$ (fast-rotating case)

Figure 13 shows the transmission and reflection coefficients for $a = 1$ and $\omega = 5$. The transmission and reflection coefficients show a larger m dependence than those for $a = 0.1$, and the boundary between perfect reflection and absorption is much deformed from an $\ell = \text{constant}$ line. This reflects the non-spherical shape of the photon sphere. The interference fringe pattern $\text{Re}[G_1]$ is elongated in the Y direction and becomes elliptic owing to the spin of the black hole. Although superradiant modes are included in the sum of the correlation function, the impact of these modes on images is not visible because the amplification factor is small for the scalar mode superradiance.

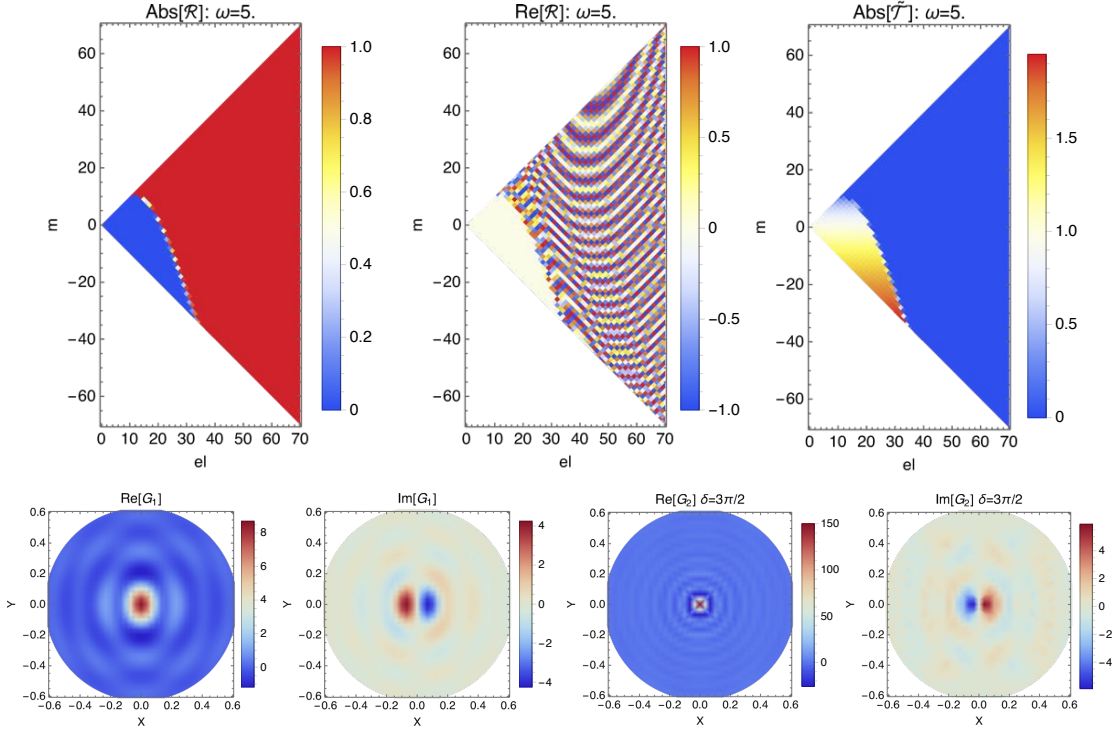


FIG. 13: Reflection and transmission coefficients in the (ℓ, m) -plane (upper panels) as well as G_1 and G_2 (lower panels) for $a = 1$ and $\omega = 5$. The interference fringe pattern $\text{Re}[G_1]$ is elongated in the Y direction and becomes elliptic because of the spin of the black hole.

Figure 14 shows images obtained from G . The image of G_1 shows a deformed D-shaped region corresponding to shape of the photon sphere. The intensity inside of the photon sphere slightly decreases as X_{im} increases because of the dragging effect of the Kerr black hole. The image of G_2 shows a dark shadow region caused by absorption of the incoming radiation from the cosmological horizon by the black hole. A peculiar feature of this image is a bright spot at the left side of the photon sphere; this enhancement of the intensity is due to the interference effect because we could not find any intensity enhancement in the image of \tilde{G}_2 . As we can see from the one-dimensional slice of images of $\mathcal{F}[G_1 + G_2]$ (right panels of Fig. 14), the right side of the photon sphere can also become bright depending on the value of δ . However, the intensity of $\mathcal{F}[G_1]$ at the left side is larger than that at the right side, and this difference is due to the dragging effect of the Kerr black hole: for $\pi\omega_+/\kappa_+ \gg 1$, the factor

$\coth(2\pi\omega_+/\kappa_+)|\tilde{\mathcal{T}}_{\ell m}|^2/\omega_+$ in the summation of G_1 is approximated to $1/\omega_+ = 1/(\omega - m\Omega_+)$. The m dependence of this factor represents the left-right asymmetry of intensity in the image because in the eikonal limit, m corresponds to the z component of photon angular momentum and is related to the screen coordinate by $m/\omega \propto -X_{\text{im}}$ [2]. The intensity of the photon sphere projected on the screen is determined by this factor after mapping m to the screen coordinate X_{im} . A positive m is mapped to a negative X_{im} , and a negative m is mapped to a positive X_{im} . From the positive direction of m (corotating direction) to the negative direction of m (counter-rotating direction), this factor decreases because of $\omega - m\Omega_+$ dependence, which is caused by the non-zero value of Ω_+ .

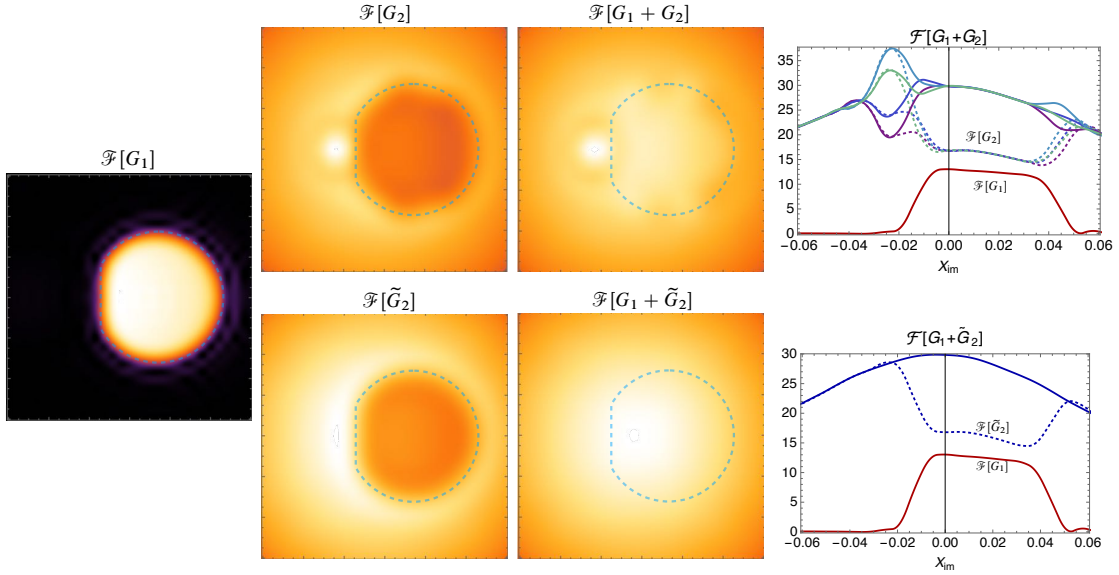


FIG. 14: Images for $a = 1$ and $\omega = 5$. Dotted circles in two-dimensional images represent the photon sphere. $\mathcal{F}[G_2]$ and $\mathcal{F}[G_1 + G_2]$ are images with $\delta = 3\pi/2$, and they show bright spots at the left side of the photon sphere, which are caused by interference between incoming and reflected modes.

Figures 15 and 16 show transmission and reflection coefficients as well as images for $a = 1$ and $\omega = 0.5$. Although we cannot identify the photon sphere in the images, the left-right asymmetry of intensity caused by the dragging effect of fast rotation of the black hole is visible.

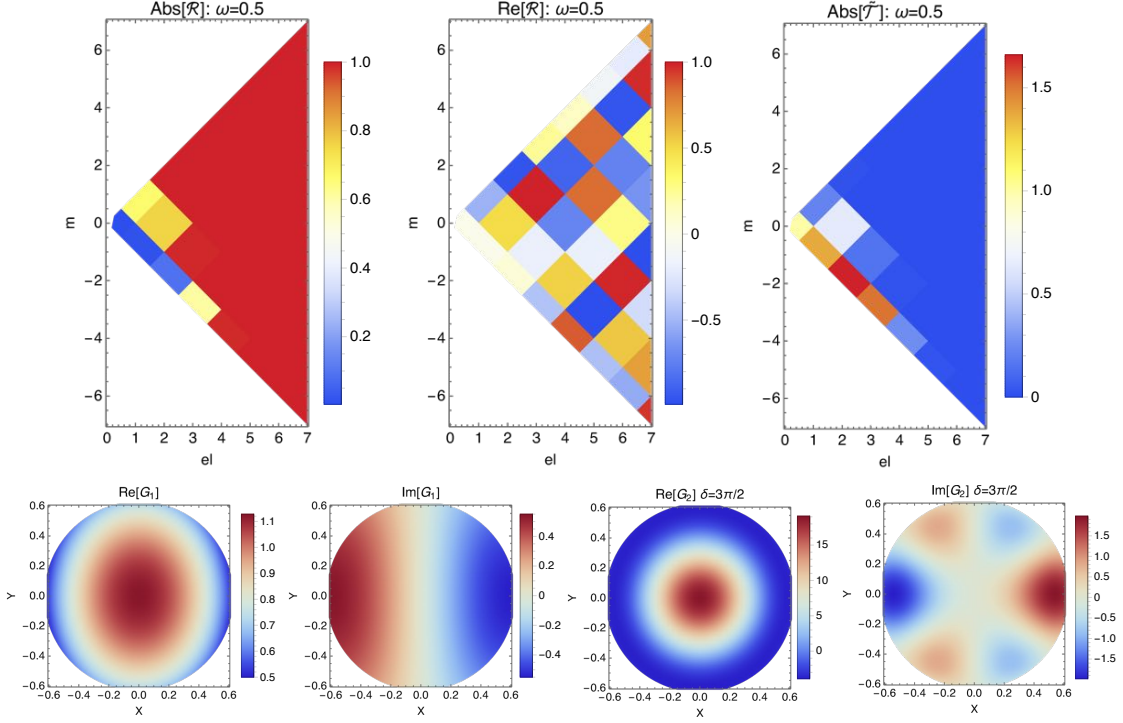


FIG. 15: Reflection and transmission coefficients in the (ℓ, m) -plane (upper panels) and G_1 and G_2 (lower panels) for $a = 1$ and $\omega = 0.5$. $\text{Im}[G_{1,2}]$ shows left-right asymmetry due to the spin of the black hole.

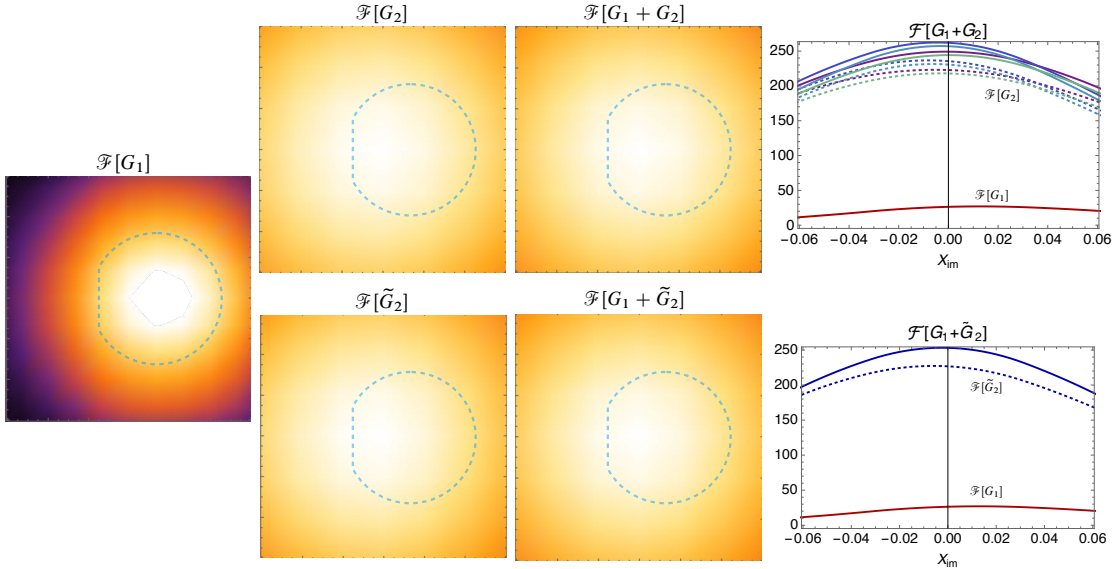


FIG. 16: Images for $a = 1$ and $\omega = 0.5$. Two-dimensional images are obtained with $\delta = 3\pi/2$. Dotted circles in two-dimensional images represent the photon sphere. $\mathcal{F}[G_2]$ and $\mathcal{F}[G_1 + G_2]$ are images with $\delta = 3\pi/2$. Left-right asymmetry is visible in the one-dimensional slice of $\mathcal{F}[G_1 + G_2]$.

4. Images of G_1 and emission region of Hawking radiation

Figure 17 shows the one-dimensional slice of images $\mathcal{F}[G_1]$ with different frequencies. For $\omega = 5$, we can identify the location of the photon sphere, which is visible as sharp edges in the image. The size of the effective emission area of Hawking radiation is the same as that of the photon sphere, as discussed in [15, 16]. For low frequency, the effective size of the radiation source obtained from the images becomes larger than the photon sphere. This is because the $\ell = 0$ mode mainly contributes to the greybody factor $|\tilde{T}_{\omega\ell m}|^2$ for $\omega \rightarrow 0$ and the characteristic size of the emission region depends on ω . The introduction of the spin of the black hole does not alter this behavior of ω dependence of the size of the emission region of Hawking radiation.

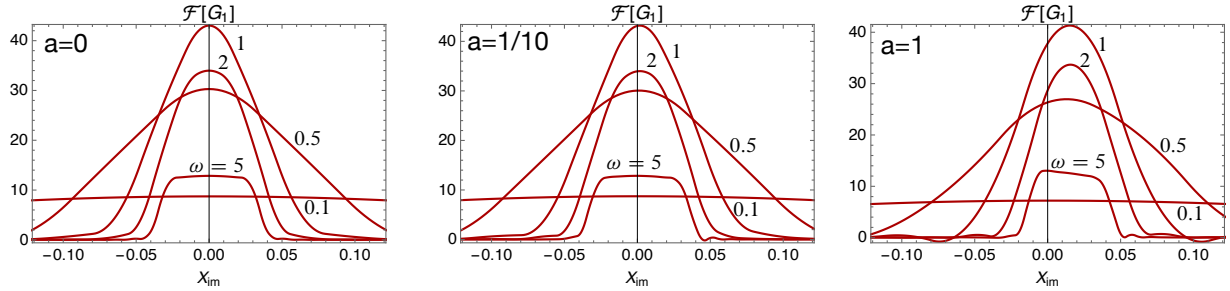


FIG. 17: Slices of images $\mathcal{F}[G_1]$ along the $Y_{\text{im}} = 0$ line. For lower frequencies, the effective size of emission region becomes larger than the photon sphere.

For obtaining black hole images directly related to the emission of Hawking radiation, we consider images of the UP mode with the correlation function $G_1 - G_1^{\text{Boulware}}$ given by Eq. (49), which subtracts contribution of the vacuum fluctuation (Fig. 18). The obtained images are sensitive to the values of the spin parameter. For $a \neq 0$, owing to the m -dependence of the Planckian factor in (49), $(e^{2\pi\omega_+/\kappa_+} - 1)^{-1} |\tilde{\mathcal{T}}_{\ell m}|^2 / \omega_+ \sim e^{-2\pi\omega_+/\kappa_+} / \omega_+$ for $\pi\omega_+/\kappa_+ \gg 1$, the intensity of the emission region around the left side of the photon sphere becomes larger and decays exponentially while departing from this region. The peak intensity of the emission region strongly depends on the spin parameter: 9.5×10^{-49} for $a = 0.1$ and 4.8×10^{-10} for $a = 1$. As this m dependence in the Planckian factor is proportional to the angular velocity of the black hole, the images of $G_1 - G_1^{\text{Boulware}}$ reflect the dragging effect in the vicinity of the event horizon of the Kerr black hole.

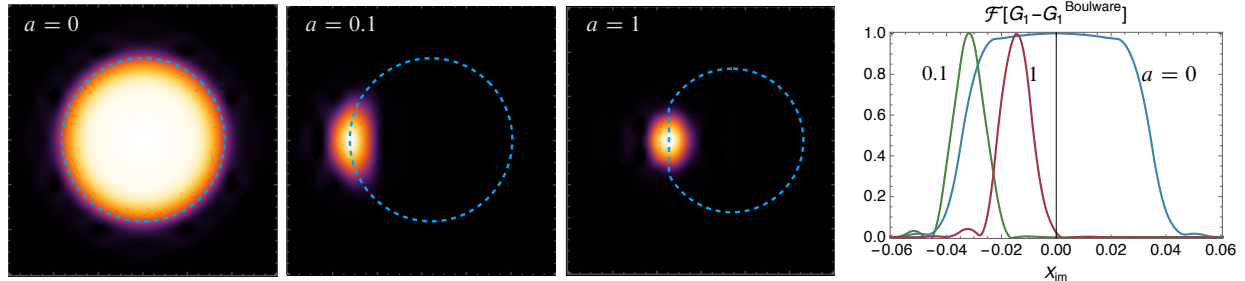


FIG. 18: Images of the UP mode for $G_1 - G_1^{\text{Boulware}}$ with $\omega = 5$. Dotted circles indicate the photon sphere. The right panel is the one-dimensional slice of images along $Y_{\text{im}} = 0$. The intensity is normalized by its peak value. The unnormalized values of the intensity are 5.1×10^{-57} for $a = 0$, 9.5×10^{-49} for $a = 0.1$ and 4.8×10^{-10} for $a = 1$.

VI. SUMMARY

We investigate the wave optical imaging of black holes using Hawking radiation. For the theoretical investigation of the imaging of astrophysical black holes, Falcke *et al.* [36] obtained images of black hole shadows using the ray tracing of photons emitted from infalling gas around a Kerr black hole. Their images show a left-right asymmetry of intensity due to the spin of the black hole and frequency dependence of images such that the “shadow” becomes invisible for low frequency because of the scattering of photons by the plasma around the black hole. Comparing their images with those obtained in the present study, the apparent structure of our images $\mathcal{F}[G_2]$ (Figs. 14 and 16) resembles theirs. However, images $\mathcal{F}[G_1 + G_2]$ show no specific structure associated with the photon sphere. As discussed in Section V A, for high-frequency waves beyond the Hawking temperature, the structure of the images $\mathcal{F}[G_1 + G_2]$ becomes flat if we neglect the interference effect. In our calculation, the adopted frequency is far higher than the Hawking temperature with $\omega_+ \approx 0.006$, $\omega_c \approx 0.008$ for $a = 1$, which is why we do not have shadow images for $\mathcal{F}[G_1 + G_2]$. Although it is not possible to identify the exact location of the wave source for Hawking radiation, we applied the van Cittert-Zernike theorem and obtained projected two-dimensional images of the black hole using the Fourier transformation of spatial correlation functions. The obtained images trace the shape of the photon sphere of the black hole for high frequency, and the black hole has appearance of a shining star with the photon sphere as its surface. For low frequency, a definite surface of emission is lost, and the emission region extends over entire field of view and is larger than the photon sphere. We found that interference between incoming modes from the cosmological horizon and modes reflected by the black hole enhances the intensity of images in the vicinity of the photon sphere for fast-spinning black holes.

We are not certain whether the “source” region of Hawking radiation is spatially incoherent, which is a crucial assumption of the van Cittert-Zernike theorem for imaging. However, although the detail of the spatial incoherence is not justified, it is possible to adopt the Fourier transformation of the spatial correlation function as a tool to visualize black holes with Hawking radiation. The spatial correlation function of the UP mode near the black hole (near the past event horizon) is roughly estimated as follows. The radial wave function

in the vicinity of the horizon is $R_{\ell m}^{\text{up}} \sim e^{-i(\omega - m\Omega)r_*}$, and

$$G_1(\theta_1, \phi_1, \theta_2, \phi_2) \sim \sum_{\ell m} |R_{\ell m}^{\text{up}}(r)|^2 S_{\ell m}(\theta_1) S_{\ell m}(\theta_2) e^{im(\phi_1 - \phi_2)} \sim \delta(\theta_1 - \theta_2) \delta(\phi_1 - \phi_2) \quad (81)$$

because $|R_{\omega \ell m}^{\text{up}}|^2$ does not have an ℓ or m dependence. Therefore, if we assume that Hawking radiation is emitted from an $r = \text{constant}$ surface in the vicinity of the horizon, the spatial coherence of that source surface is zero and we have justified the applicability of the van Cittert-Zernike theorem to imaging with Hawking radiation. The emission region of Hawking radiation may differ from the vicinity of the horizon, and for such a case, we cannot make assertions on the spatial incoherence of the source region of Hawking radiation. The spatial coherence of the source will result in hazy images, and more rigorous investigation on the spatial coherence of Hawking radiation will reveal its ‘‘quantumness’’. The word ‘‘quantumness’’ is obscure, and we should properly define it based on entanglement. If we reconsider the van Cittert-Zernike theorem for a source with spatial coherence, it may be possible to access information on the degree of coherence of Hawking radiation. This direction of investigation is related to entanglement harvesting in black hole spacetimes with the method of intensity correlation [37], and we will report on this subject in a separate publication.

Acknowledgments

Y.N. was supported in part by JSPS KAKENHI Grant No. 19K03866.

Appendix A: Van Cittert-Zernike theorem in de Sitter spacetime

In this Appendix, we consider the van Cittert-Zernike theorem in de Sitter spacetime with the metric

$$ds^2 = -f dt^2 + \frac{dr^2}{f} + r^2 d\Omega^2, \quad f = 1 - \frac{\Lambda}{3} r^2, \quad \Lambda > 0. \quad (A1)$$

A massless conformal scalar field Φ obeys

$$\left(\square - \frac{R}{6} \right) \Phi = 0, \quad R = 4\Lambda, \quad (A2)$$

and the scalar field is separated as

$$\Phi = e^{-i\omega t} \frac{R_\ell(r)}{r} Y_{\ell m}(\theta, \phi). \quad (A3)$$

The radial wave equation is

$$\left[\frac{d^2}{dr_*^2} + \omega^2 - \frac{\ell(\ell+1)H^2}{\sinh^2(Hr_*)} \right] R_\ell(r_*) = 0, \quad Hr = \tanh(Hr_*), \quad H^2 = \frac{\Lambda}{3}, \quad (A4)$$

where $r_* = \int dr/f$ is the tortoise coordinate. The Green’s function for Eq. (A2) is given by

$$\mathcal{G}_\omega(\mathbf{x}, \mathbf{x}_s) = \frac{i\omega}{4\pi r r_s} \sum_{\ell} R_\ell^{(1)}(r_{s*}) R_\ell^{(2)}(r_*) (2\ell+1) P_\ell(\mathbf{n} \cdot \mathbf{n}_s), \quad (A5)$$

where $\mathbf{x} = r_* \mathbf{n}$ and $\mathbf{x}_s = r_{s*} \mathbf{n}_s$ with $|\mathbf{n}| = |\mathbf{n}_s| = 1$, and $R_\ell^{(1)}$ is regular at $r = 0$, and $R_\ell^{(2)}$ is outgoing at $r_* = \infty$. We assume $\ell/\omega \ll 1/H$, which means that the ‘‘impact parameter’’ of the wave mode with ℓ is smaller than the Hubble horizon length and that the effect of the cosmological constant is negligible. Under this condition, for $r_{s*} \ll 1/(\omega H)$, $R_\ell^{(1)}(r_{s*}) \sim r_{s*} j_\ell(\omega r_{s*})$, and for $1 \ll \omega r_*$, $R_\ell^{(2)}(r_*) \sim (-i)^{\ell+1} e^{i\omega r_*} / \omega$. Thus, the Green’s function behaves as

$$\begin{aligned} \mathcal{G}_\omega(\mathbf{x}, \mathbf{x}_s) &\propto \frac{e^{i\omega r_*}}{r} \sum_\ell (2\ell + 1) (-i)^\ell j_\ell(\omega r_{s*}) P_\ell(\mathbf{n} \cdot \mathbf{n}_s) \\ &= \frac{1}{r} \exp[i\omega(r_* - \mathbf{x} \cdot \mathbf{x}_s / r_*)]. \end{aligned} \quad (\text{A6})$$

This Green’s function corresponds to (3) for the case of flat space. The only difference is that the radial coordinate is replaced with the corresponding tortoise coordinate. Therefore, the van Cittert-Zernike theorem for de Sitter spacetime has the same form as the flat case with the replacement $r \rightarrow r_*$ in the phase factor.

-
- [1] V. P. Frolov and I. D. Novikov, *Black Hole Physics* (Kluwer Academic Publisher, Dordrecht, Netherlands, 1998).
 - [2] V. P. Frolov and A. Zernikov, *Introduction to Black Hole Physics* (Oxford University Press, 2011).
 - [3] E. Teo, ‘‘Spherical photon orbits around a Kerr black hole’’, *General Relativity and Gravitation* **35**, (2003) 1909-1926.
 - [4] The Event Horizon Telescope Collaboration, ‘‘First M87 Event Horizon Telescope Results. I. The Shadow of the Supermassive Black Hole’’, *Astrophys. J.* **875**, (2019) L1.
 - [5] The Event Horizon Telescope Collaboration, ‘‘First M87 Event Horizon Telescope Results. II. Array and Instrumentation’’, *Astrophys. J.* **875**, (2019) L2.
 - [6] The Event Horizon Telescope Collaboration, ‘‘First M87 Event Horizon Telescope Results. III. Data Processing and Calibration’’, *Astrophys. J.* **875**, (2019) L3.
 - [7] The Event Horizon Telescope Collaboration, ‘‘First M87 Event Horizon Telescope Results. IV. Imaging the Central Supermassive Black Hole’’, *Astrophys. J.* **875**, (2019) L4.
 - [8] The Event Horizon Telescope Collaboration, ‘‘First M87 Event Horizon Telescope Results. V. Physical Origin of the Asymmetric Ring’’, *Astrophys. J.* **875**, (2019) L5.
 - [9] The Event Horizon Telescope Collaboration, ‘‘First M87 Event Horizon Telescope Results. VI. The Shadow and Mass of the Central Black Hole’’, *Astrophys. J.* **875**, (2019) L6.
 - [10] M. Born and E. Wolf, *Principles of Optics* (Cambridge University Press, 1999), 7th ed.
 - [11] E. Wolf, *Introduction to the theory of coherence and polarization of light* (Cambridge University Press, 2007).
 - [12] K. Sharma, *Optics: principles and applications* (Academic Press, Tokyo, 2006).
 - [13] S. W. Hawking, ‘‘Black hole explosions?’’, *Nature* **248**, (1974) 30–31.
 - [14] S. W. Hawking, ‘‘Particle creation by black holes’’, *Commun. Math. Phys.* **43**, (1975) 199–220.
 - [15] S. B. Giddings, ‘‘Hawking radiation, the Stefan-Boltzmann law, and unitarization’’, *Phys. Lett. B* **754**, (2016) 39–42.
 - [16] R. Dey, S. Liberati, and D. Pranzetti, ‘‘The black hole quantum atmosphere’’, *Phys. Lett. B* **774**, (2017) 308–316.

- [17] K.-i. Kanai and Y. Nambu, “Viewing black holes by waves”, *Class. Quantum Gravity* **30**, (2013) 175002.
- [18] Y. Nambu and S. Noda, “Wave optics in black hole spacetimes: the Schwarzschild case”, *Class. Quantum Gravity* **33**, (2016) 075011.
- [19] W. G. W. Unruh, “Notes on black-hole evaporation”, *Phys. Rev. D* **14**, (1976) 870–892.
- [20] P. Candelas, “Vacuum polarization in Schwarzschild spacetime”, *Phys. Rev. D* **21**, (1980) 2185–2202.
- [21] A. C. Ottewill and E. Winstanley, “Renormalized stress tensor in Kerr space-time: General results”, *Phys. Rev. D* **62**, (2000) 1–15.
- [22] R. Gregory, I. G. Moss, N. Oshita, and S. Patrick, “Black hole evaporation in de Sitter space”, *arXiv:2103.09862* .
- [23] N. D. Birrell and P. C. W. Davies, *Quantum fields in curved space* (Cambridge University Press, 1984).
- [24] B. Reznik, “Entanglement from the vacuum”, *Found. Phys.* **33**, (2003) 167–176.
- [25] A. Pozas-Kerstjens and E. Martín-Martínez, “Harvesting correlations from the quantum vacuum”, *Phys. Rev. D* **92**, (2015) 064042.
- [26] L. J. Henderson, R. A. Hennigar, R. B. Mann, A. R. H. Smith, and J. Zhang, “Harvesting entanglement from the black hole vacuum”, *Class. Quantum Gravity* **35**, (2018) 21LT02.
- [27] Y. Nambu and Y. Ohsumi, “Classical and quantum correlations of scalar field in the inflationary universe”, *Phys. Rev. D* **84**, (2011) 044028.
- [28] A. Matsumura and Y. Nambu, “Violation of Bell-CHSH Inequalities through Optimal Local Filters in the Vacuum”, *Quantum Reports* **2**, (2020) 542–559.
- [29] G. Vidal and R. Werner, “Computable measure of entanglement”, *Phys. Rev. A* **65**, (2002) 032314.
- [30] E. Tjoa and R. B. Mann, “Harvesting correlations in Schwarzschild and collapsing shell spacetimes”, *J. High Energy Phys.* **2020 (8)**, (2020) 155.
- [31] G. Menezes, “Entanglement dynamics in a Kerr spacetime”, *Phys. Rev. D* **97**, (2018) 85021.
- [32] S. Akcay and R. A. Matzner, “The Kerr–de Sitter universe”, *Class. Quantum Gravity* **28**, (2011) 085012.
- [33] Y. Hatsuda, “Quasinormal modes of Kerr–de Sitter black holes via the Heun function”, *Class. Quantum Gravity* **38**, (2021) 025015.
- [34] H. Motohashi and S. Noda, “Exact solution for wave scattering from black holes: Formulation”, *Prog. Theor. Exp. Phys.* **2021 (8)**, (2021) 1–27.
- [35] H. Suzuki, E. Takasugi, and H. Umetsu, “Perturbations of Kerr-de Sitter Black Holes and Heun’s Equations”, *Prog. Theor. Phys.* **100**, (1998) 491–505.
- [36] H. Falcke, F. Melia, and E. Agol, “Viewing the Shadow of the Black Hole at the Galactic Center”, *Astrophys. J.* **528**, (2000) L13–L16.
- [37] G. Baym, “The physics of Hanbury Brown-Twiss intensity interferometry: From stars to nuclear collisions”, *Acta Phys. Pol. B* **29**, (1998) 1839–1884.